AA2024/SiC metal matrix composites simultaneously improve ductility and cracking resistance during elevated temperature deformation

O.V. Rofman [a,b,*], A.V. Mikhaylovskaya [a], A.D. Kotov [a], A.G. Mochugovskiy [a], A.K. Mohamed [a,c], V.V. Cheverikin [a], M.P. Short [d,e]

[a] Department of Physical Metallurgy of Non-Ferrous Metals, National University of Science and Technology MISiS, Moscow, 119049, Russian Federation
[b] Laboratory of Radiation Materials Science, Institute of Nuclear Physics, Almaty, 050032, Kazakhstan
[c] Shoubra Faculty of Engineering, Benha University, Cairo, 11629, Egypt
[d] Department of Nuclear Science and Engineering, Massachusetts Institute of Technology, Cambridge, MA, 02139, USA
[e] Moscow Engineering Physics Institute (MEPhI), Moscow, 115409, Russian Federation

A B S T R A C T

This study uses the stir-casting technique to combine a semi-solid AA2024 alloy directly with finely-sized β-SiC$_p$ embedded as a powder or with mechanically alloyed granules as a delivery agent. Liquid-state primary fabrication tends to form agglomerates of reinforcement particles, whereas rolling better distributes the composite constituents. Sub-micron reinforcements of low volume fractions do not significantly increase the hardness of the composite materials. Uniaxial tensile testing at elevated temperatures over a wide range of strain rates showed simultaneous increases in the ductility and crack resistance of AA2024 + SiC$_p$ granules embedded as a powder when compared to the non-reinforced control material at lower strain rates, with the same toughness as the control material. The maximum engineering strain of 252.7 $\pm$ 19.2% was observed in AA2024/SiC$_p$ at a strain rate of 10^{-4} s^{-1}. This improvement in properties is attributed to grain refinement in the MMCs, leading to pinning events during the straining and ductility increases. The resultant impediments to grain growth and crack propagation allow the fine-sized reinforcements to control dynamic microstructural changes during fatigue. Cube {001}<100> is a dominant texture component in AA2024, whereas the Goss {011}<100> and S {123}<634> components mainly represent the texture of the discontinuously reinforced aluminum matrix.

1. Introduction

The development and study of metal-matrix composites (MMCs) represents a challenging and rewarding task in the field of material science, as they have the potential for useful combinations of mechanical properties which cannot be achieved using conventional alloys. Modification of different light alloys with reinforcing constituents provides a direct, practical route to fabricating light-weight composite materials by imparting new properties such as increased elastic modulus, high wear resistance, and increased ultimate tensile stress at required ductility levels. Incorporation of fine ceramic particles can refine the grain structure in the MMC matrix [1–4] to achieve these beneficial mechanical properties. The right choice of matrix alloy, reinforcement volume fraction and size (*micro and/or nanosized reinforcements*), morphology (*fibers, whiskers, particulates, or in combination*), and their specific physical characteristics (*thermal expansion, thermal conductivity*) will determine the resulting properties of the MMC. The production technology and thermomechanical processing will partially determine the feasibility of using the MMC in a finished product. Research activities and industrial applications of Al-, Ti-, and Mg-based MMCs has significantly evolved over the past 25 years, as documented by Clyne (1993) [5], Miracle (2005) [6], and Srivatsan et al. (2018) [7]. Nowadays, laboratory-scale research aims to test different concepts *ex situ* and *in situ* to increase applications of MMCs [8]. For example, a few specific, industrial-scale studies have been performed to create metal-carbon nanotube composites [9] and to employ them as radiation resistant materials [10]. Different additive manufacturing approaches have also been used to develop MMC printing strategies for specialized applications [11–13]. A number of industrial companies (e.g., Rio Tinto Alcan [14,15], Materion [16–18]and

Alvant [19]) as well as emerging start-ups (e.g., Gamma Alloys [20,21]) specialize in industrial scale MMC research, development, and production.

At present, many primary fabrication routes conventionally used for large-scale production of alloys are not applicable for many types of MMCs. This is one of the reasons that prevents their widespread use in industry. Major technological limitations are often attributed to difficulties with adding ceramic dispersoids to liquid metals, inhomogeneous distribution of reinforcements in the matrix, increased melt viscosity (which has a substantial, negative effect during casting), and chemical reactions at the reinforcement–matrix interface [22]. In some cases, the given obstacles are explained by the physical nature of the material constituents, such as a high contact angle between the aluminum matrix and SiC_p [23]. One example of such an effect is the difference in the coefficients of thermal expansion between the reinforcement components and the matrix, which often results in the development of residual stresses at metal/particulate interfaces. Another aspect is the process used to fabricate MMCs. The attractiveness of liquid-phase fabrication techniques of MMCs is associated with the minimization of energy costs to produce large amounts of material. At the same time, liquid-phase processing routes [24], such as *stir casting, infiltration,* or *spray casting* are influenced by low wettability of some ceramic constituents, such as SiC and Al_2O_3 (contact angle $> \pi/2$). This deteriorates the incorporation of reinforcements into the molten matrix metal, leading to their inhomogeneous distribution and clustering [25–27]. The problem is acutely expressed for the case of nanosized ceramic particles, when the reinforcement/matrix interface area is large. A number of processing methods have been proposed to overcome the above-mentioned difficulties, e.g., *pneumatic powder injection, ultrasonic-assisted fabrication, squeezing,* and *centrifugal casting* [28–31]. However, one should consider that sonication and centrifugal casting may lead to significant design complexities for large-scale facilities. Additional obstacles are related to the capture of the gas atmosphere and slag during mechanical stirring, intensive oxidation of reinforcements, and void or microdefect formation. The creation of the required protective atmosphere and the development of refinement techniques that do not target reinforcements are also needed to improve the casting quality of MMCs.

Powder metallurgy methods such as *mechanical alloying, reaction milling, cryomilling,* and *microwave and spark plasma sintering* help to exclude low-wettability aspects attributed to liquid-state processing [22, 28,32,33]. Solid-state processes provide an opportunity to incorporate a large volume fraction of reinforcements into the matrix and to combine different components, which are not suitable for processing MMCs following liquid-state routes. Nevertheless, the questions relevant to the amount of energy required for milling, compacting/extrusion stages, uniform distribution of reinforcements (especially nanosized), porosity, and proper interfacial bonding should still be addressed. A detailed review on different approaches for mixing and homogeneous distribution of nanoparticles is given in Ref. [34] Several relatively new processing technologies to produce MMCs based on *spray atomization and deposition* [35,36], *friction stir processing* [37], *powder injection molding* [38], *equal channel angular pressing* [39], and *roll-bonding* [40,41] confirm new developments in this direction.

Besides primary MMC fabrication routes, subsequent thermomechanical processing is an important stage that shapes the resulting properties of the material. The rolling conditions of MMCs are determined by the consolidated effect of the matrix alloy and different characteristic factors attributed to the reinforcement particles. For example, the effect of the size and volume fraction of SiC_p on the evolution of the microstructure in aluminum alloys was addressed by Humphreys et al. in Ref. [42]. The study pays attention to cold rolling, particle-stimulated nucleation (PSN) and pinning effects, recovery and recrystallization phenomena, as well as grain growth in particulate reinforced composites. The impact of deformation on ceramic particles is discussed in terms of the fracture and realignment of ceramic reinforcements. In a related work [43], the authors discussed the strengthening mechanisms that govern the changes in mechanical characteristics of MMCs during thermomechanical processing. Detailed studies on the deformation (yielding behavior and elastic response) of discontinuously reinforced MMCs were performed by Prangnell et al. [44,45]. The effect of deformation by torsion on dynamic recovery/recrystallization of AA2024 with different volume fractions of SiC_p is given in Ref. [46]. The interesting aspects of the resultant superplastic behavior of MMCs are documented in Refs. [22,47–49].

This study aims to contribute to the growing area of research on MMCs by exploring improvements in mechanical properties and microstructural changes during high-temperature, uniaxial tensile testing of AA2024/β-SiC_p reinforced with fine-sized β-SiC_p particulates. AA2024 is the basis for this research as one of the more common, high-strength 2xxx series alloys. The alloy is well studied and widespread in the industry (mainly for high-strength structural applications) because of its high strength-to-weight ratio, good formability, and dispersoid hardening response to heat treatment. AA2024 is also in demand for products for which high durability in tension is required [50]. However, 2xxx wrought alloys are characterized by fair general or stress corrosion cracking resistance (based on exposures to sodium chloride solution) compared to other aluminum alloys, owing to a greater change in electrode potential with variations in the amount of Cu in solid solution [51]. They have low tribological properties [52], and AA2024 is less ductile at elevated temperatures ($\sim 0.6 T_{melt}$) compared to that of superplastic aluminum-based alloys [49].

In this paper, we study how the incorporation of fine-sized ceramic reinforcements by different methods changes the mechanical characteristics of AA2024-based MMCs at elevated temperatures. We quantify changes in mechanical performance obtained from uniaxial tensile testing of AA2024/β-SiC_p and strain characteristics at different temperatures and strain rates. The effect of adding SiC_p dispersoids on deformation-induced microstructural changes is discussed. Scanning and transmission electron microscopy (SEM)/(TEM) and energy-dispersive X-ray spectroscopy (EDS) analysis are performed to describe intermetallic phases formed in the matrix. Electron backscatter diffraction (EBSD) analysis is performed to estimate the effect of SiC_p dispersoids on grain structure and substructure development during deformation. It is found that embedding a low volume fraction of reinforcement particulates has a positive effect on grain refinement during thermomechanical processing, keeping grain sizes smaller by pinning grain boundaries. Along with the uniformly distributed fine-sized intermetallic particles, this consistently influences dynamic recovery and slows down dynamic grain growth (DGG). This is considered as a good prerequisite to control grain size and increase ductility, the application of which is seen in improved hot workability and superplastic forming of MMCs at high strain rates. The results of this study demonstrate that a properly processed AA2024 MMC can exhibit enhanced ductility, and cracking resistance with retained toughness compared to conventional alloys, opening the door to the more widespread use of MMCs in the correct industrial settings.

2. Material and methods

AA2024 commercial alloy (Al–4.2Cu–1.3Mg–0.6Mn–0.23Fe–0.5Si, wt.%) was used as a matrix material. The alloy was melted in a clay-graphite crucible in a Nabertherm K4/13 furnace at 700°C. The temperature of the melt was controlled by a K2 chromel–alumel thermocouple and associated temperature controller. The melt was then slowly cooled to 620–640°C. The temperature interval was chosen close to the solid-liquid range, which in addition to enabling mechanical stirring facilitates the incorporation of reinforcements in the vortex. Two approaches were used to disperse the SiC_p reinforcement constituent in the alloy melt. In the first case, β-SiC_p powder with a high volume fraction of fine-sized particles (D90 = 530 nm, i.e. 90% of the particles are 530 nm or smaller) was delivered in portions to the melt surface. The second variant was employed to introduce mechanically alloyed (AA2024+β-

SiC_p) granules[1] of 10% volume fraction and a mean size of 54 μm as a carrier agent of SiC_p to the alloy melt. Reinforcements were introduced in portions and accompanied by mechanical stirring for several minutes. The four-blade impeller was made of a Ti alloy to reduce dissolution of constituent elements when immersed in the melt. Stirring was maintained until the addition of reinforcement was completed, and then the slurry was reheated to 750°C and cast into a water-cooled copper mold $20 \times 40 \times 100$ mm^3 in size. The cooling rate in the mold was approximately 15 K/s. High volume fractions of reinforcements require preheating molds as well as squeeze casting to provide a uniform distribution of SiC in the ingot. Homogenization annealing on the as-cast materials was performed in two stages, following a typical AA2024 heat treatment procedure; annealing at 380°C for 8 h (formation of fine precipitates) followed by 490°C at 14 h (elimination of dendrite liquation).

Homogenized ingots were then hot rolled (T = 420 °C, ε_{HR} ~0.6) and cold rolled (ε_{CR} ~0.85) to a sheet thickness of 1.2 mm using a reversing DUO-250 two-roll mill with steel rolls 230 mm in diameter. The rolling process was undertaken at 0.24 m/s. The rolling strain per pass was ~0.02. To maintain the temperature during the hot rolling stages, the samples were kept for approximately 3 min in the furnace before each pass to reheat to the rolling temperature. After the thermomechanical treatment, MMC sheets were annealed at T = 490 ± 5°C for 5 min in a salt bath to recrystallize the structure and limit the stage of grain growth. AA2024 alloy cast and thermo-mechanically processed under the same condition was used as a reference material to compare the resulting properties. Differential scanning calorimetry (DSC) was conducted using a LABSYS ATD-DSC (Setaram Instrumentation) employing a heating/cooling rate of 20°C/min for a range of 20–400°C and 5°C/min for 400–700°C. The samples were placed in corundum (Al_2O_3) crucibles in an air atmosphere (cast materials) and in an Ar atmosphere (AA2024/SiC MA granules). An identical, empty corundum crucible was used as the reference. The DSC thermograms were corrected by subtracting the baseline obtained with an empty crucible following the same heating/cooling procedure.

Mechanical properties and microstructural evolution were estimated at intermediate stages. The Vickers hardness was characterized following the ASTM E92 standard. A Wilson Wolpert Vickers indenter with a load of 5 kg for 15 s was used to evaluate the hardness. At least 15 measurements were recorded per sample. At least 15 measurements were recorded per sample. Uniaxial tensile testing was conducted at 450°C and 490°C at constant strain rates of 10^{-1}, 10^{-2}, 10^{-3}, and 10^{-4} s^{-1} in a Walter + Bai AG LFM 100 kN testing machine equipped with a high-temperature, three-section chamber and operated with the commercial Dion Pro software. ASTM E2448-18 was used as reference standard to evaluate the superplastic properties of the metallic sheet materials. To maintain a constant strain rate, the traverse speed was increased as the test samples elongated. Before loading, the specimens were heated in the chamber and maintained at the deformation temperatures for 20 min. Tensile samples were prepared along the rolling direction using a DK77 spark erosion machine (current did not exceed 2 A). The tensile sample gauge dimensions of $14.0 \times 6.0 \times 1.2$ mm corresponded to the length (l_0), width (w_0), and thickness (t_0). Sample gauge dimensions were selected following GOST 1497 (ISO 6892 analogue), where $l_0 = 5.65 \times \sqrt{w_0 \times t_0}$. Square tag ends, instead of standard samples with the transition radius between the gripped ends

and the parallel length of the gauge section, were used for all the experiments to determine the superplastic characteristics. The data from two to three specimens were collected for each tensile condition. After testing, the deformed samples were rapidly removed from the chamber and quenched in water to attain room temperature.

Sectioned and mounted samples were mechanically ground using standard silicon carbide 600-, 1200-, 2400-, and 4000-grit abrasive papers in conjunction with water lubricant. Each abrasive size was used for several minutes at low pressure to produce a flat surface. Specimens were cleaned between each stage to prevent contamination by abrasive particles. Final polishing was performed using a 40 nm OP-U colloidal silica suspension. To estimate the surface quality, a Carl Zeiss Axiovert 200 M MAT light microscope was used under different illuminations including polarized light. For preliminary estimation of the grain size of the rolled or deformed samples, the microstructure was revealed by anodizing (16 V, 0–5°C) using Barker's reagent (HBF$_4$ (46 ml), HBO$_3$ (7 g), and H$_2$O (970 ml)). Specimens for electron microscopy studies were electropolished using a CH$_3$OH + HNO$_3$ solution (volume ratio 7:3). The process was conducted at a temperature of −30 °C for 10 s with an applied DC potential of 12 V.

Detailed microstructural studies were performed using a Vega3 TESCAN 3LMH SEM with a LaB$_6$ filament. The SEM was equipped with an X-MAX 80 EDS detector (Oxford Instruments) and an electron backscatter diffraction system (HKL NordlysMax, Oxford Instruments). SEM imaging was performed at an accelerating voltage of 20 kV in secondary-electron (SE) mode and backscattered electron (BSE) mode at working distances of 10–15 mm. EDS analysis was carried out on representative areas of interest by acquiring point spectra or selected area mapping. Fine reinforcement particles, precipitates, and dislocation structure were analyzed by TEM using a JEOL JEM 2100 at 200 kV. EDS data were collected in STEM mode by an X-Max detector (Oxford Instruments). EBSD data were obtained at 20 kV using beam scan mapping (AZtecHKL) to control the position of the electron beam within the field of view. The step size was chosen to be 0.5 μm for the selected area of 278×278 μm^2. The acquired data were analyzed by the in-house Vmap program [53] and the HKL EBSD post-processing software [54]. The EBSD maps obtained from the non-deformed regions of AA2024/β-SiC$_p$ tensile samples contained more than 85% indexed points (aluminum). The EBSD maps collected from the deformed regions (particularly at high strain rates) and failure areas were characterized by a lower percentage of indexed data. This was attributed to distortion of the crystal structure, development of cracks, and presence of SiC$_p$ clusters. The definition of a high-angle grain boundary was set with a lower limit of 15° misorientation (HAGBs, shown in black on the EBSD maps), and all boundaries below this limit (down to 2°) were classified as low-angle grain boundaries (LAGBs, shown in grey on the EBSD maps).

3. Results

3.1. As-cast and homogenized microstructure

Fig. 1 illustrates as-received β-SiC$_p$ particles and AA2024+SiC$_p$ MA granules and optical micrographs of the as-cast structures of AA2024 alloy, AA2024/SiC$_p$ (powder, 2 vol %), and AA2024/SiC$_p$ (10 vol %, AA2024+SiC$_p$ granules). BSE images at higher magnification and EDS elemental mapping can be found in the supplementary materials (Fig. S1). The microstructure of the matrix alloy consists of cored dendrites of an aluminum solid solution with various constituents in the inter-dendritic regions. As shown in the figures below, a clustering of SiC$_p$ powder is observed in the as-cast material (Fig. 1e), whereas the granules are separately distributed (Fig. 1f). This example of an Al–Cu–Mg/SiC system shows significant difficulties to introduce, distribute, and retain dispersed reinforcement particles in the melt. The approach, based on embedding powder particles directly into the matrix alloy, is associated with high surface tension of the Al$_2$O$_3$ film and low wettability of the ceramic. The difference in the densities of AA2024

---

[1] Mechanical alloying (MA) of AA2024 powder with β-SiC$_p$ nanosized particles was conducted in a Retsch PM400 planetary ball mill using a stainless steel vial and balls (16 mm in diameter, 16.2 g each) under an argon environment. The ball-to-powder weight ratio was 10:1. MA was performed at a speed of 300 rpm for 6 h where each milling interval of 5 min was followed by a 5 min break. No process control agent was used during MA. The chosen milling regime is applicable only for low-volume fractions of SiC, as its further increase leads to intensive cold welding due to the high heat capacity of SiC.
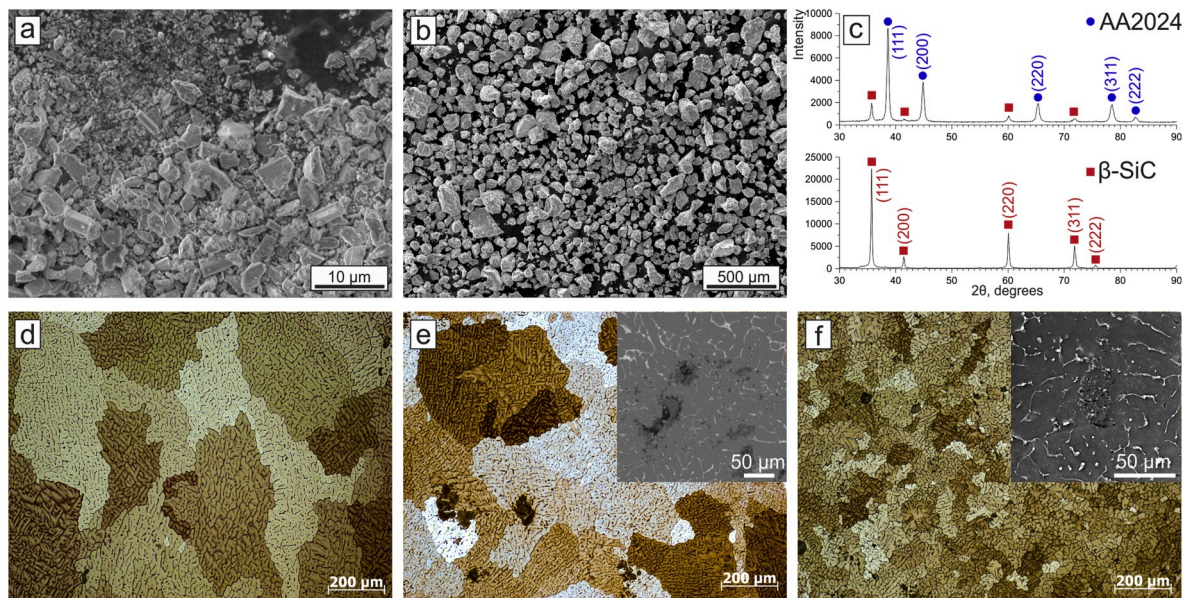
Fig. 1. SEM micrographs of (a) β-SiC$_p$ and (b) AA2024+SiC$_p$ MA granules and (c) corresponding X-ray diffraction spectra. Optical images (in polarized light) of as-cast materials: (d) AA2024 alloy, (e) AA2024/SiC$_p$ (2 vol %, powder), (f) AA2024/SiC$_p$ (10 vol %, AA2024+SiC$_p$ MA granules).

(2.78 g/cm^{-3}) and SiC (3.16 g/cm^{-3}) also plays a dual role: the oxide Al$_2$O$_3$ film results in the floating of SiC$_p$ whereas a consolidated introduction of powder particles (e.g. as a briquette) leads to their settling. Nevertheless, negative influences of these factors can be minimized. As a preliminary stage, it is recommended to use preheated powder to prevent the melt from cooling and to eliminate residual moisture. If injecting is not used, the powder can be sieved in the process of its introduction into the melt. These procedures seek to reduce the presence of large clusters in the slurry during primary fabrication stages. The semisolid temperature interval facilitates embedding SiC$_p$ by changing rheological properties of the melt by increasing its viscosity, owning to the transformation to a dendritic structure [55]. An overview of the different processing techniques designed to overcome the difficulties of incorporating and dispersing the discontinuous reinforcements within an aluminum alloy matrix is presented in Ref. [56].

The applied homogenization treatment mostly eliminated dendritic liquefaction in the matrix, and stimulated reprecipitation of the solute as fine and more uniformly distributed second-phase particles. This reflects the role of secondary phases in the formation of the initial microstructure and properties of the material which further evolve during subsequent thermomechanical processing. In AA2024 the concentration of Cu and Mg exceeds the maximum solubility of these elements in solid solution. The type of soluble compounds (containing Cu, Mg, Si, or their combination) is controlled by both concentrations of elements and their weight ratio. A Cu content exceeding 2 wt % leads to the formation of θ-Al$_2$Cu, whereas Mg > 0.5 Si results in the introduction of Mg atoms with the S–Al$_2$CuMg phase. The presence of Fe and Mn leads to the nucleation of Al$_6$CuFe (if Fe » Si) or Al$_{20}$Cu$_2$Mn$_3$ and T-Al$_{12}$CuMn$_2$ (if Mn » Fe) phases. Formation of Al$_6$(FeMn) [50,57] and Al$_{12}$(FeMn)$_3$Si phases can also be observed and is presented in the following sections. These nanosized dispersoids, formed as a result of solid-phase interactions during heat treatment, is more resistant to growth and, in addition to θ-Al$_2$Cu and S–Al$_2$CuMg, they control evolution of the grain structure. Annealing improved the hot workability of the cast ingots and provided uniformity of the properties. The optimal solution treatment also provides greater improvements to the tensile properties and reduces the fatigue crack growth rates [58].

Unlike secondary phases, which show an increase in size or volume fraction resulting from temperature or strain, the SiC$_p$ reinforcements are more resistant to this effect at the given temperatures. Fig. 2a shows

SEM images of the as-cast, homogenized microstructure of the AA2024 matrix reinforced with SiC$_p$ (2 vol %, powder). It is confirmed by EDS elemental mapping that both fine SiC$_p$ particles and separately distributed, coarse ceramic reinforcements are present in the microstructure. The presence of the oxide layer on the surface of SiC$_p$ can be considered from a number of aspects. Firstly, oxidized SiC$_p$ acts as a source for additional oxidation of the AA2024 melt. The effect of a silica layer on wettability is discussed in detail in Ref. [59,60], and despite an observed decrease in the contact angle, it is both governed by the process duration and temperature, and limited by the strong reactivity between SiO$_2$ and aluminum. The reactivity of SiC reinforcements has another aspect: a reaction of SiC and molten aluminum by the following chemical process 3SiC(s) + 4Al(1) → Al$_4$C$_3$(s) + 3Si(s) [61]. The reaction takes place intensively at temperatures exceeding 1073 K, but the formation of Al$_4$C$_3$ was also observed at the melting point of Al [60,62–64]. Therefore, in the given temperature interval, SiO$_2$ may react more efficiently as a protective layer.

Fig. 2b illustrates the changes occurring in the matrix of AA2024 reinforced with (AA2024+SiC$_p$) MA granules (10 vol %). An option to use MA granules as a "delivery agent" resolves the problem of wettability, facilitates dispersoid incorporation, and reduces the time to accommodate particulates in the melt. It is apparent from this figure that MA granules are more uniformly distributed in the matrix of the homogenized material compared to the distribution of the fine-sized SiC$_p$ powder. EDS analysis confirms slight changes in the granules in the alloy after casting and subsequent heat treatment. On one hand, this is considered as a possibility to provide a local hardening for the material. However, a special attention should be paid to their size; large granules may significantly reduce cold workability and ductility of the material. For example, strong and brittle granules that kept their original size due to the presence of an Al$_2$O$_3$ protective layer will not be able to restrain grain growth in the matrix and will play a role of stress concentrators during straining. One of the ways to eliminate this drawback is to produce fine-sized MA granules far smaller than the mean grain size of the matrix alloy. An increase of the volume fraction of the granules and the use of an inert, protective environment may impart a significant improvement in the properties of MMCs.
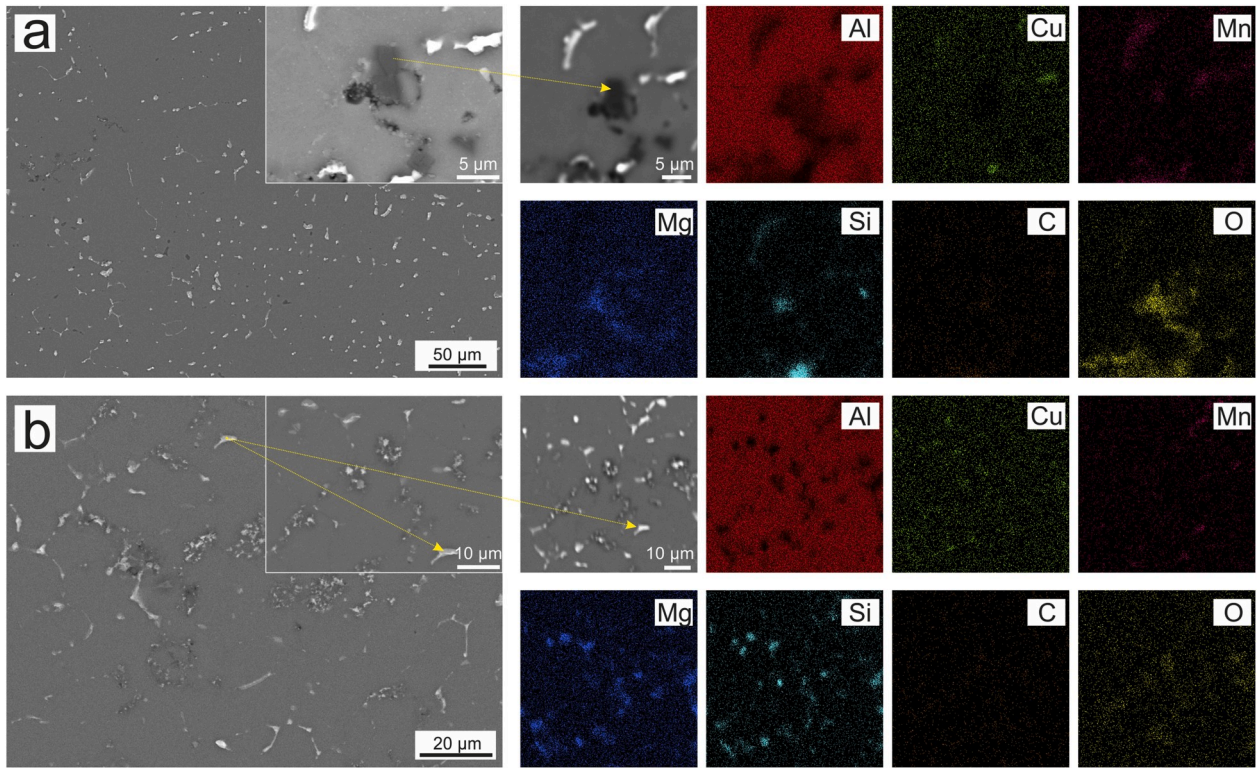
Fig. 2. SEM images and relevant EDS maps of homogenized AA2024 (380°C/8 h + 490°C/14 h) reinforced with SiC$_p$ (2 vol %), which were introduced into the matrix as (a) a powder and (b) AA2024+SiC$_p$ MA granules.

3.2. As-rolled microstructure, DSC analysis, and hardness measurements

The baseline, homogenized AA2024 alloy and AA2024-based MMCs underwent rolling in two stages. Hot rolling at 420°C provided acceptable loading for the rolling mill to break down the cast structure into a wrought one, reduced the impact of high temperature on the developing grain structure. At the given temperature, the thickness decreased from 20 mm to 8 mm by reaching 60% reduction (rolling strain per pass was ~0.02), and the materials demonstrated good ductility. Subsequent processing to a sheet thickness of 1.2 mm by cold rolling provided an additional reduction of 85% to obtain a refined grain structure in the matrix. Fig. 3 illustrates the rolled and recrystallized microstructure of the AA2024 alloy and its modification by SiC$_p$, as well as the DSC thermograms (in the temperature range of 400–700 °C) of the processed
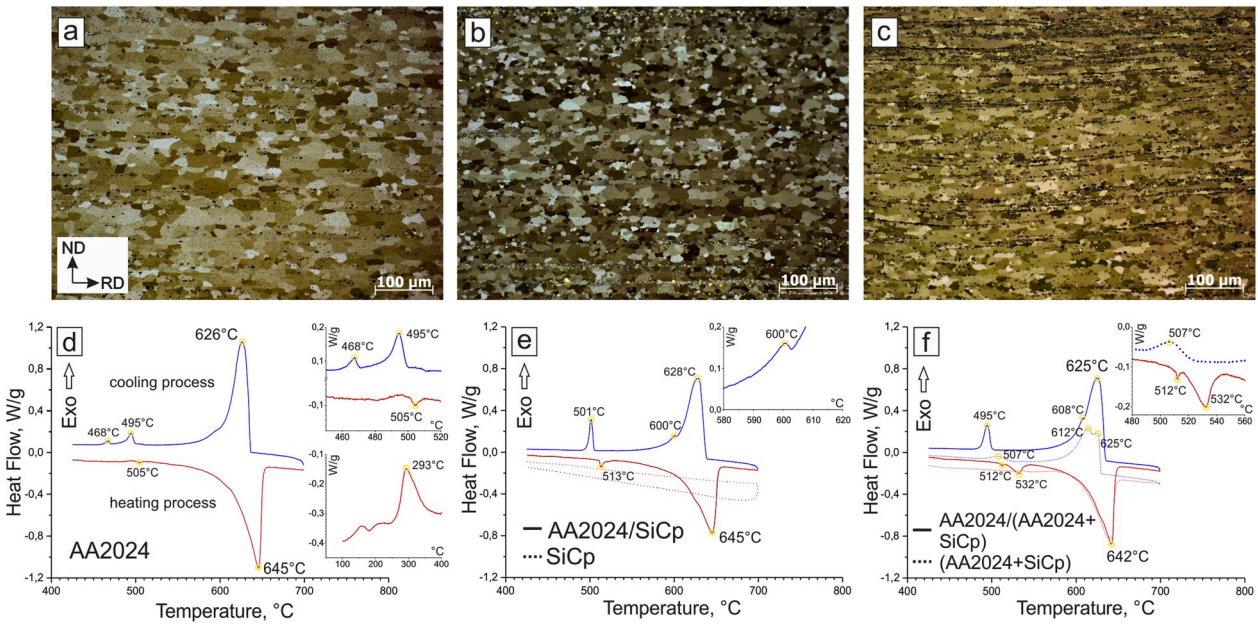

Fig. 3. Optical images of the rolled (ε_{HR} ~0.6 + ε_{CR} ~0.85) and recrystallized (490°C/5 min in salt bath) microstructure of (a) AA2024 alloy, (b) AA2024/SiC$_p$ (2 vol %, powder), and (c) AA2024/SiC$_p$ (10 vol %, AA2024+SiC$_p$ MA granules). DSC scans from (d) AA2024, (e) AA2024/SiC$_p$ and SiC$_p$, and (f) AA2024/(AA2024+SiC$_p$) and AA2024+SiC$_p$ MA granules.

materials and their constituent components.

As can be seen from Fig. 3a–c, the microstructure of the MMCs is characterized by a slightly lower mean grain size (~7 μm) than that of the AA2024 alloy (~10 μm). This could be attributed to the effect of reinforcing particles causing easier nucleation of new, recrystallized grains, thus limiting excessive grain growth in later stages of heat treatment. Stages of hot and cold rolling generate a high density of dislocations. The presence of dispersoids as well as SiC_p increases the amount of dislocations and obstructs their movement, retaining a finer-grained structure at subsequent stages of recrystallization annealing. In addition to the development of the desired microstructure, thermo-mechanical treatment performs another important function related to the segregation of secondary phases and reinforcement particles. Liquid-state primary fabrication tends to form agglomerates of reinforcement particles, whereas rolling better distributes the composite constituents. The same effect was observed during rolling of extruded Al-Cu-Mg [65, 66]. More evidence is available concerning the positive effects of mechanical processing on the homogeneous distribution of the reinforcements [56] and the healing effects of metal flow [67]. The major disadvantage is a linear arrangement of ceramic particles in the rolling direction.

DSC thermograms, obtained using the same heating and cooling rates as those used for sample manufacture (Fig. 3d–f), reflect the major phase transformations occurring in the heat treated AA2024 matrix and in its behavior in the presence of reinforcement particles. Comparative DSC scans for SiC_p and AA2024 + SiC_p MA granules in the given temperature interval are also presented. The response from the matrix alloy at the first stage of heating (up to 400°C) is characterized by the following sequence of phase transformations, related to aging [68]: original supersaturated solid solution (α_0) → α_1 + Guinier-Preston (GP) zones → α_2 + metastable θ'' → α_3 + θ' → α_4 + stable θ (Al_2Cu) phase and α_0 → α_1 + GP zones → α_2 + S' → α_3 + stable S (Al_2CuMg) phase, where α_i is the composition of the matrix in equilibrium with the relevant second phase. The most pronounced exothermic peak centered at 293°C (AA2024) is likely attributed to the formation of a semi-coherent θ' phase (the process is accompanied by a parallel exothermic transformation to create S' phase) followed by their subsequent dissolution (Fig. 3d). The presence of SiC_p in the matrix at this stage is characterized by a larger degree of peak spreading and overlapping, as well as shifted peak maxima towards lower temperatures (Table 1). Formation of the stable θ (Al_2Cu) and S (Al_2CuMg) phases takes place between 470 and 480°C. The endothermic peak observed at ~505 °C indicates partial melting of the matrix alloy resulting from the dissolution of Cu-rich phases. SiC_p (Fig. 3e) and AA2024+SiC_p MA granules (Fig. 3f) shift the maximum of this endothermic process to ~513 °C. An increase in peak temperature for AA2024/(AA2024+SiC_p) is also accompanied by the additional absorption of energy (Fig. 3f) indicated by the peak centered at 532 °C. It can be explained by the delay of the partial melting in the MA granules.

Table 2 shows the hardness values of the as-cast, homogenized, and rolled materials. The maximum hardness in the as-cast condition was obtained for powder-reinforced AA2024/SiC_p (2 vol %). Homogenization annealing resulted in strengthening due to the formation of a supersaturated solid solution of Cu and Mg in Al and fine dispersoids in the microstructure. Rolling with subsequent short-term recrystallization annealing slightly decreased the hardness values. From the obtained

Table 2
HV_5 hardness of AA2024 alloy and AA2024/SiC_p measured at different processing stages.

Processing stage/Material	Vickers hardness, HV_5		
	AA2024	AA2024/SiC_p (2 vol %, powder)	AA2024/SiC_p (10 vol %, MA granules)
As-cast	90.7 ± 3.3	107.9 ± 7.1	97.2 ± 4.4
Homogenization annealing (380°C/8 h + 490°C/14 h)	135.4 ± 4.9	129.6 ± 3.2	111.2 ± 3.7 (134.2 for areas with granules)
Rolling and recrystallization (490°C/5 min)	122.2 ± 2.5	126.4 ± 3.6	120.8 ± 4.6

data, it follows that sub-micron reinforcements of low volume fractions do not significantly increase the hardness. Girot et al. [56] indirectly support this conclusion by stating that large reinforcing particles are more effective against abrasive wear on the MMC than smaller ones.

3.3. High-temperature tensile testing

Uniaxial tensile testing at elevated temperatures was conducted to evaluate plastic and strength characteristics of the investigated AA2024-based materials. Experiments were conducted at 450 °C and 490 °C, the latter of which is close to the solidus for AA2024, and constant strain rates of 10^{-1}, 10^{-2}, 10^{-3}, and 10^{-4} s^{-1}. Fig. 4 shows the true stress–true strain diagrams of the studied materials, and Table 3 provides the tensile testing data analysis. It is worth mentioning that we applied a constant strain rate when the samples deformed uniformly without necking. As the length of the deformed part increased, the strain rate increased as well to keep the strain rate constant.

At elevated temperatures and high and intermediate strain rates, AA2024 is characterized by low engineering strain (58.3–122.5%). The maximum ductility (179.3 ± 28.4%) for the given conditions for AA2024 is achieved at 10^{-4} s^{-1} (490°C). The strain rate sensitivity index m varies from 0.20 ± 0.01 (450°C) to 0.27 ± 0.03 (490°C), which reflects low aptitude of this alloy for superplasticity. AA2024/SiC_p (2 vol %) reinforced with fine-sized powder exhibits similar strains (69–118.3%) at high and intermediate strain rates. The maximum engineering strain (252.7 ± 19.2%) for this material was observed at a strain rate of 10^{-4} s^{-1}. The m value varies from 0.21 ± 0.01 (450°C) to 0.33 ± 0.02 (490°C), which is considered as an opportunity to improve the ductility of composite materials at temperatures close to the temperature of solidus for the matrix alloy. The most pronounced effect of the increase in the ductility by reaching superplasticity levels was observed in a number of studies [49] by reinforcing the studied alloy with *whiskers*. The volume fraction of reinforcements can reach 20% and still provide high-strain rate superplasticity. AA2024/SiC_p (10 vol %, MA granules) showed minimal values of engineering strain (21–104%) of the studied materials for the given testing conditions. During the test of this material, crack formation often occurred because of high-volume fraction of composite granules. This resulted in failure at the early stages of testing. At the same time, the m value was 0.22 ± 0.01 (450°C) and 0.33 ± 0.02 (490°C). It could be concluded that AA2024+SiC_p MA granules have the potential for distribution of strengthening

Table 1
Thermal properties and heat effects associated with corresponding DSC peaks (the heating cycle, T_S, T_L and T_m are the solidus, liquidus, and melting temperatures).

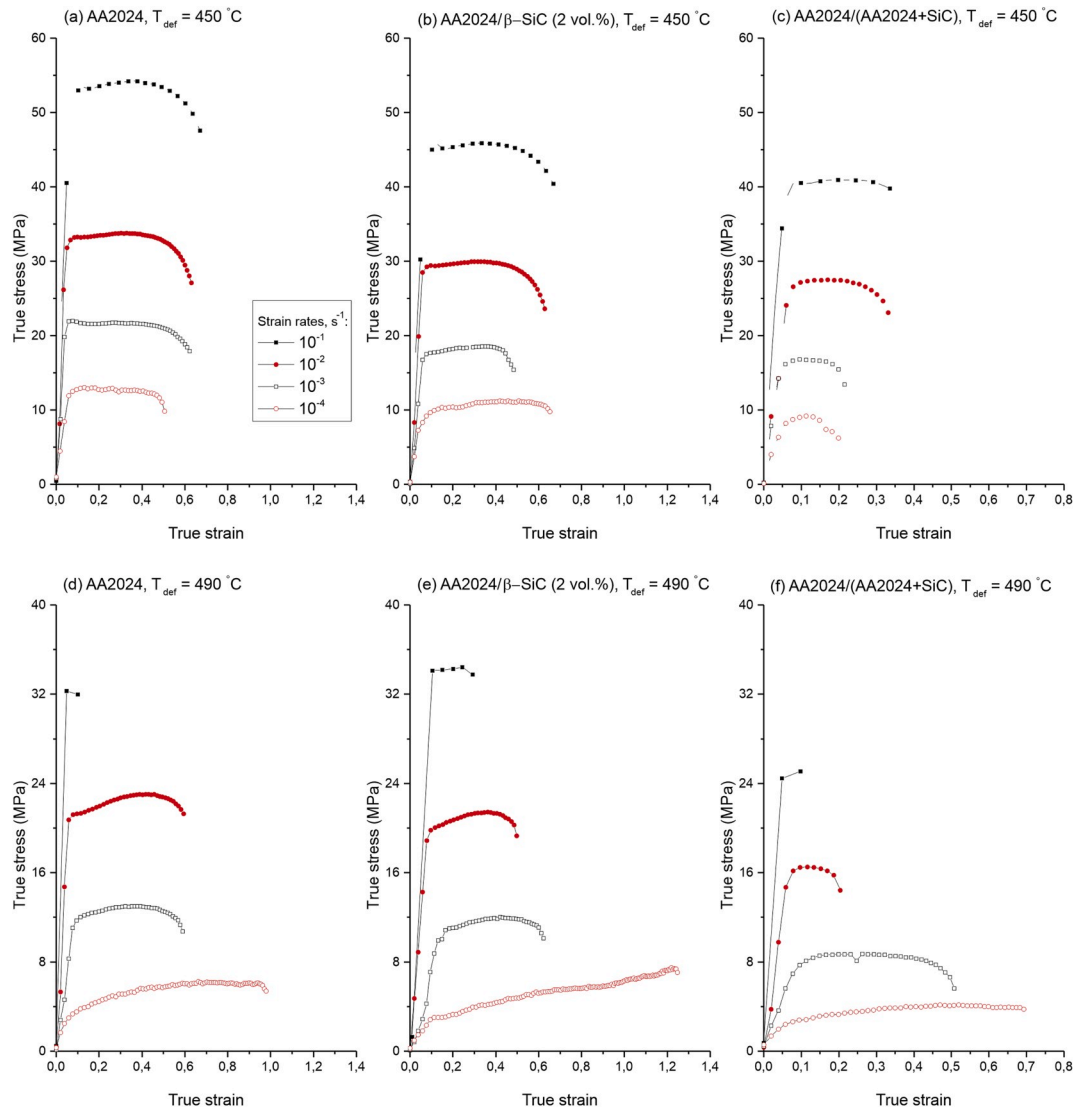| Material	DSC Peak Temperature, °C			Change of enthalpy (ΔH, J/g) at the given peak temperature (T_p, °C)					
	T_S	T_m	T_L	T_p	ΔH	T_p	ΔH	T_p	ΔH
AA2024	510	645	657	293	9.31	505	−0.06	645	−27.41
AA2024/SiC_p	540	645	660	288	1.77	513	−0.29	645	−19.51
AA2024/(AA2024+SiC_p)	545	642	654	267	1.56	513, 532	−0.05, −1.00	642	−20.46
AA2024+SiC_p MA granules	590	648	660	230	3.57	550, 588	–	648	−14.10

Fig. 4. Effect of the strain rate (10^{-1}, 10^{-2}, 10^{-3}, and 10^{-4} s^{-1}) and testing temperature (450 °C and 490 °C) on the true stress–strain characteristics of (a, d) AA2024 alloy, (b, e) AA2024/SiC_p (2 vol %), and (c, f) AA2024/(AA2024 + SiC_p).

components in the matrix. However, more attention should be paid to their preparation process, size, volume fraction, and elimination of linear arrangements to improve ductility.

3.4. Deformation-induced microstructural changes at elevated temperatures

The effect of temperature and deformation on grain growth in the AA2024/SiC_p (2 vol %) is demonstrated by EBSD orientation maps obtained after uniaxial tensile testing in Fig. 5a–d. Related boundary misorientation plots for the testing conditions are given in Fig. 5g and h. The mean grain size in the non-deformed regions does not exceed 7 μm (450 °C) and 8 μm (490°C) depending on the straining regimes. The grain structure of AA2024/SiC_p in the non-deformed regions is characterized by relative stability to the effect of the temperature and does not significantly evolve during the test (Table 4, Fig. 5a, d). For the deformation-affected areas, grain growth caused by the deformation (*DGG* [69,70]) was observed for all strain rates and testing temperatures. The measured grain size is given in Table 4 and observed in Fig. 5b and c (450 °C) and 5e-f (490 °C).

It is worth noting that DGG occurs for the given composite materials at relatively modest rates even at 490 °C. It is likely caused by the presence of fine β-SiC_p particulates and a high fraction of second-phase dispersoids. This in turn helps the material to resist grain growth by *Zener pinning* [71,72] even during the perturbation of pinning events during deformation, thus reaching high strains at low strain rates. Coarse particles are additional sources for stress accumulation, which may stimulate the formation of a substructure with further dynamic recovery and recrystallization. The effect of the temperature and strain rate is reflected by the formed substructure (Table 4, Fig. 5g and h). At 450°C, regardless of strain rate, where intensive development of LAGBs (up to 26%) is observed in the deformed regions. The substructure development at 490°C is more rate-sensitive. Testing at low strain rates (10^{-4} s^{-1}) results in almost a four-fold decrease in LAGBs (to 6.5%) formed during the deformation, and at given conditions this parameter is close to a non-deformed structure. An intermediate stage of LAGB formation during high strain rate testing is shown in Fig. 5j and k. It illustrates inhomogeneity of plastic deformation due to high stress concentration near coarse particles as well as in some grains characterized by a high amount of dislocations.

Fig. 6a–d shows changes in the grain size of the non-deformed (static grain growth) and deformed (DGG) parts of the AA2024 and AA2024/(AA2024+SiC_p) samples. Grain boundary misorientation plots for the given testing conditions are given in Fig. 6e and f. A continuous

Table 3

Data of tensile strength and toughness, elongation, and strain rate sensitivity of AA2024 and SiC_p reinforced composites at room and elevated temperatures. For elevated temperatures, data are given first as ranges tested at 450 °C before the slash, then as ranges tested at 490 °C.

Material	ε', s^{-1}	T_{25}, °C					ε', s^{-1}	T_{450}/T_{490}, °C				N
		$R_{p0.2}$, MPa	R_m, MPa	ε_f, %	u_t, MJ/m^3	N		$R_{p0.2}$, MPa	ε_f, %	u_t, MJ/m^3	m	
AA2024	4.7×10^{-3}	303 ± 8	465 ± 19	7.4 ± 1.4	42 ± 9	2	10^{-1}	54.3 ± 1.5 36.3 ± 5.1	**117.7** ± 22.2 **58.1** ± 21.6	54.4 ± 11.8 20 ± 9.7	$0.20 \pm 0.01/0.27 \pm 0.03$	4/4
							10^{-2}	35 ± 2.8 23.0 ± 2.8	122.5 ± 4.9 83.5 ± 12.0	38.6 ± 5.8 18 ± 0.2		2/2
							10^{-3}	21 ± 1.4 14 ± 4.2	99 ± 4.2 92 ± 2.1	17.7 ± 2.4 10 ± 0.8		2/2
							10^{-4}	11.7 ± 0.6 3.5 ± 0.6	103.8 ± 16.7 **179.3** ± 28.4	11.1 ± 2.2 10 ± 2.6		4/4
AA2024/2% SiC_p	4.7×10^{-3}	268 ± 21	351 ± 55	3.1 ± 1.7	19 ± 9	2	10^{-1}	45.7 ± 1.2 33.3 ± 1.2	**118.3** ± 3.2 **69** ± 17.5	46.2 ± 2.1 18.6 ± 5.1	$0.21 \pm 0.01/0.33 \pm 0.02$	4/4
							10^{-2}	28.3 ± 2.1 19.5 ± 0.7	106 ± 21.9 86 ± 25.5	23.7 ± 3.7 14.9 ± 0.3		2/2
							10^{-3}	19.5 ± 2.1 11.5 ± 2.1	92 ± 19.8 104 ± 29.7	14.5 ± 3.2 10 ± 0.4		2/2
							10^{-4}	8.5 ± 0.9 2.7 ± 0.5	**124.7** ± 19.7 **252.7** ± 19.2	11.9 ± 1.9 13.4 ± 2.5		4/4
AA2024/(AA2024 + 10% SiC_p)	4.7×10^{-3}	270 ± 1	312 ± 12	1.3 ± 0.2	9 ± 1	2	10^{-1}	40/24	**58**/21	19/3	$0.22 \pm 0.01/0.33 \pm 0.02$	1/1
							10^{-2}	26/16	73/37	12/4		1/1
							10^{-3}	16/8	30/88	4/5		1/1
							10^{-4}	8/3	**30**/104	2/4		1/1

List of symbols: ε' – strain rate, s^{-1}; T_{25} – room temperature (25 °C); T_{450} – elevated tensile temperature (450 °C); T_{490} – elevated tensile temperature (490 °C); $R_{p0.2}$ – yield strength, MPa; R_m – ultimate tensile strength, MPa; ε_f – elongation to failure, %; u_t – tensile toughness, MJ/m^3; m – strain rate sensitivity index; N – number of samples tested at the given conditions.

temperature effect (490°C) results in the slower increase of the mean grain size for AA2024/SiC_p (Fig. 5d) and AA2024/(AA2024+SiC_p) (Fig. 6c) MMCs compared to that for the AA2024 alloy (Fig. 7a). Besides some difference in the initial microstructure (caused by the effect of reinforcement particles on the development of grain structure during thermomechanical treatment), the difference in the grain size resulted from the pinning effect from the reinforcement particles on grain boundary movement. Dynamic grain growth demonstrates a similar tendency. It is observed in all strained materials at the given temperature and testing rates (Figs. 5f and 6d), but its maximum rate is reached for the AA2024 alloy (Fig. 6b).

The anisotropy of the mechanical properties of the MMC is mainly attributed to the size, morphology, and spatial distribution of the reinforcements. In case of a low volume fraction of the hard phase, the crystallographic texture developed in the soft matrix is assigned a significant role in the overall anisotropic response. The texture of rolled AA2024 is generally characterized by heavy textures of Cube, Goss, and S components [73]. Deformation texture plays a significant role in determining the orientation of the material during further processing. Information on the crystallographic texture was derived from EBSD maps of AA2024/SiC_p (Fig. 7a–d), AA2024 (Fig. 7e and f), and AA2024/(AA2024+SiC_p) (Fig. 7g and h). Orientation distribution function (ODF) data were used to evaluate the main texture components in the recrystallized samples. The EBSD orientation maps (Fig. 7) and the corresponding ODF (Fig. S2) indicate that the recrystallization texture consisted of several components with a range of orientations, such as the Cube {001}<100>, Goss {011}<100>, and S {123}<634> components. It can be seen that Cube (e.g. $\phi_1 = 0°$, $\Phi = 0°$ $\phi_2 = 0°$) is a dominant texture component in AA2024, whereas Goss (e.g. $\phi_1 = 0°$, $\Phi = 45°$ $\phi_2 = 0°$) and S (e.g. $\phi_1 = 59°$, $\Phi = 37°$ $\phi_2 = 63°$) components mainly represent the texture of the discontinuously reinforced aluminum matrix. This observation is partly supported by Ref. [74], who showed that a hard phase, introduced into an aluminum alloy, does not modify the main components of the texture. It has also been observed that the texture levels for the reinforced materials are weaker than those for the matrix alloy. However, the particle size should be considered:

fine particles (<0.1 μm) provide homogeneous deformation and a more pronounced texture intensity in reinforced materials than non-reinforced materials, whereas large particles lead to a more heterogeneous deformation and consequently to a decrease in the texture intensity. As expected, the tensile testing resulted in a weakened texture due to dynamic recrystallization.

Fig. 8 shows defects formed near the fracture zone, and presents EDS maps acquired from the area with coarse secondary particles after high-strain rate testing (10^{-1} s^{-1}) at 490°C. At intermediate strain rates, the formation of cracks with no further development was detected on the stress–strain diagrams. It is seen from the figure that cracks mainly form in SiC_p clusters, but do not increase intensively. β-SiC_p particulates introduced into the matrix are also characterized by surface oxidation. It is explained by the tendency of SiC to form a passivation layer of SiO_2 at elevated temperatures. The presence of a fraction of fine-sized β-SiC_p results more intense oxidation [75,76], including in the given temperature interval, during stir casting. The EDS analysis performed in the area of β-SiC_p localization reveals a higher concentration of Mg. This can be attributed to the formation of the Mg_2Si phase specific for concentrations of Mg>0.9% and Si>0.5% [77]. Coarse intermetallic precipitates are θ-Al_2Cu and S–Al_2CuMg phases. A small volume fraction of a coarse (Al, Fe, Si, Mn) constituent phase was also observed.

3.5. Fine structure (TEM) in AA2024/SiC_p

TEM studies of the deformed structure were carried out to investigate the distribution of β-SiC_p particulate and second-phase dispersoids in the AA2024 matrix. Figs. 9–11 show TEM images and EDS element maps (Fig. 9a and b and Fig. 10a and b) acquired from samples deformed at different conditions. Generally, second-phase precipitates in AA2024 are represented by several major groups [78]: θ-Al_2Cu, Al_2CuMg, and $Al_{12}(FeMn)_3Si$ (hardening precipitates of rounded or irregular shape), and complex intermetallic dispersoids of the $Al_{20}Cu_2Mn_3$ (or T-$Al_{12}CuMn_2$) and Al_6MnFe (or $Al_6CuMnFe$) systems. It was reported that stoichiometric ratios for some constituent phases may vary significantly [79,80]. The size of fine, Mn/Fe enriched dispersoids for the initial
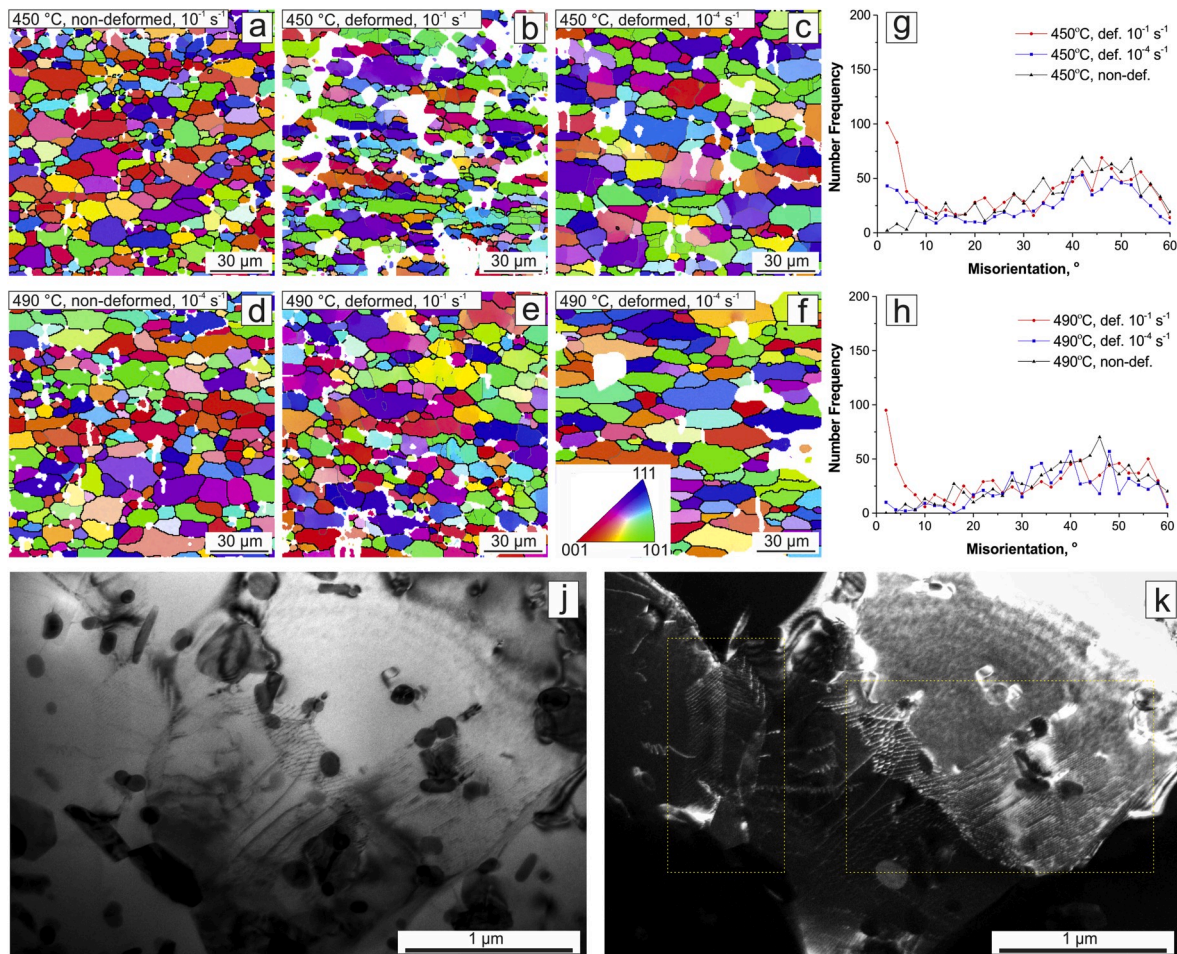
Fig. 5. Illustration of DGG in the matrix of AA2024/SiC$_p$ using (a–f) EBSD maps in the Inverse Pole Figure (IPF) colors and distribution plots of boundary misorientation for different strain rates and temperatures (g) 450 °C and (h) 490 °C. White color on the EBSD maps indicates unindexed points, which represent clusters of reinforcement/large precipitates or defects/cracks formed during deformation; the tensile direction is parallel to the *x* axis. TEM images (j) bright field and (k) weak beam dark field, which illustrate parallel *screw dislocations* and *dislocation walls* in the AA2024/SiC$_p$ sample deformed at 10^{-1} s^{-1} at 450 °C. (For interpretation of the references to color in this figure legend, the reader is referred to the Web version of this article.)

Table 4
Mean grain size and fraction of LAGBs in AA2024/SiC$_p$ (2 vol %), AA2024/(AA2024 + SiC$_p$) and AA2024 after high-temperature uniaxial testing at different strain rates.

Testing temperature, °C	Strain rate, s^{-1}	Mean grain size, μm		LAGBs, %	
		non-deformed	deformed	non-deformed	deformed
AA2024					
490	10^{-4}	10 ± 0.6	14.0 ± 1.2	9.8	12.4
AA2024/SiC$_p$ (2 vol %)					
450	10^{-1}	6.9 ± 2.3	10.1 ± 4.3	8.5	26.7
	10^{-4}	7.1 ± 1.8	11.2 ± 3.3	5.1	23.1
490	10^{-1}	6.1 ± 1.7	8.9 ± 2.9	5.6	23.3
	10^{-4}	8.0 ± 3.2	11.4 ± 2.5	4.4	6.5
AA2024/(AA2024 + SiC$_p$)					
490	10^{-4}	6.6 ± 1.8	9.8 ± 3.2	2.6	3.1

material does not exceed 200 nm and is characterized by an *elliptical* or *rod-like* morphology. They are formed during long-term homogenization annealing and are uniformly distributed in the matrix. During static annealing and deformation, they help to restrain grain growth by the *Zener pinning* mechanism. A similar function to reduce the migration rate

of the grain boundaries is performed by β-SiC$_p$ located both at the grain boundaries (Fig. 9c) and in the matrix.

The joint effect of the high temperature (490°C) and deformation leads to an increase in precipitate size. As a result, this may reduce their pinning force on the grain boundaries.

It was observed that during deformation, fine dispersoids of Al$_6$(FeMn) phases are linked by dislocation helices (Fig. 9d and e and Fig. 11). It is considered that particles become obstacles for further movement of dislocations during straining. In addition to dislocation helices, samples deformed at high strain rates are characterized by the presence of wavy dislocations. At high strains, intersection of slip systems results in the development of dislocation walls, which contribute to further evolution of the substructure.

4. Discussion

Major findings of this research show that modification of AA2024 by SiC$_p$ leads to the refinement of microstructure and deceleration of DGG at elevated temperatures. At near-solidus temperatures, the deformed powder-reinforced MMC demonstrates higher elongation at a low strain rate and provides better performance at a high strain rate compared to that for the matrix alloy, all while retaining the toughness of the matrix material. The obtained data give evidence of the resistance of fine-sized reinforcements to the propagation of cracks. With respect to the obtained results, an attempt was performed to analyze the contributing
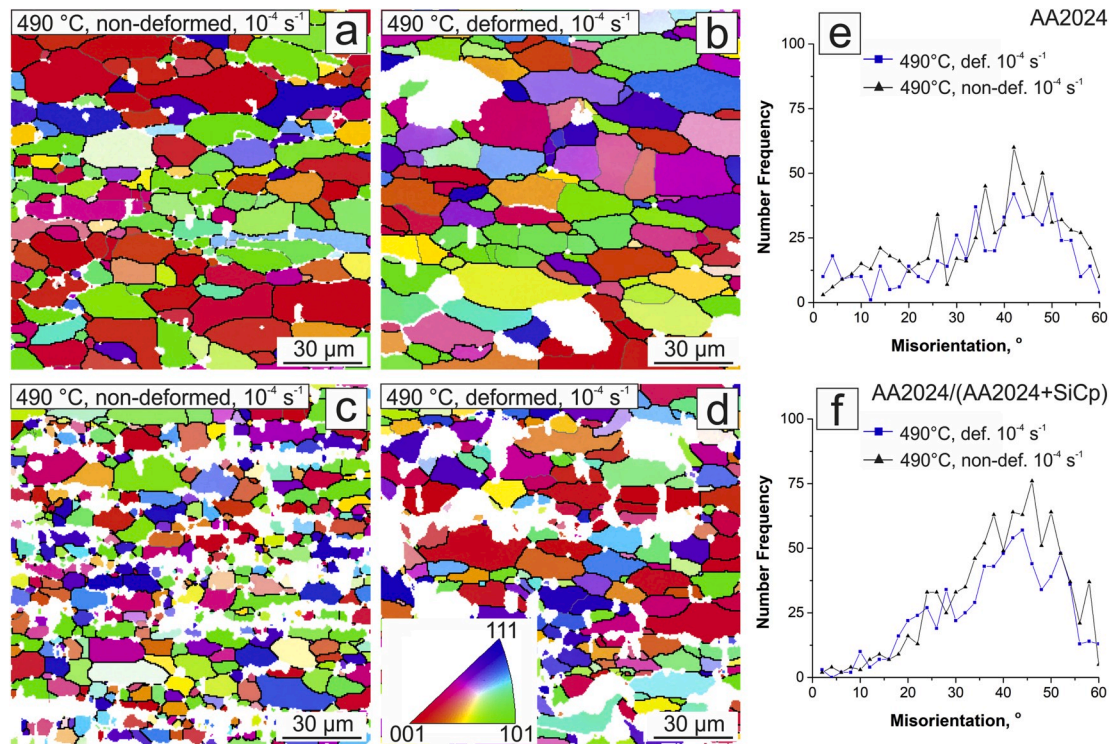
Fig. 6. EBSD maps (IPF colors) and distribution plots of boundary misorientation for the non-deformed and deformed regions of (a, b, e) AA2024 alloy and (c, d, f) AA2024/(AA2024+SiC$_p$) deformed at 10^{-4} s^{-1} (490 °C). (For interpretation of the references to color in this figure legend, the reader is referred to the Web version of this article.)
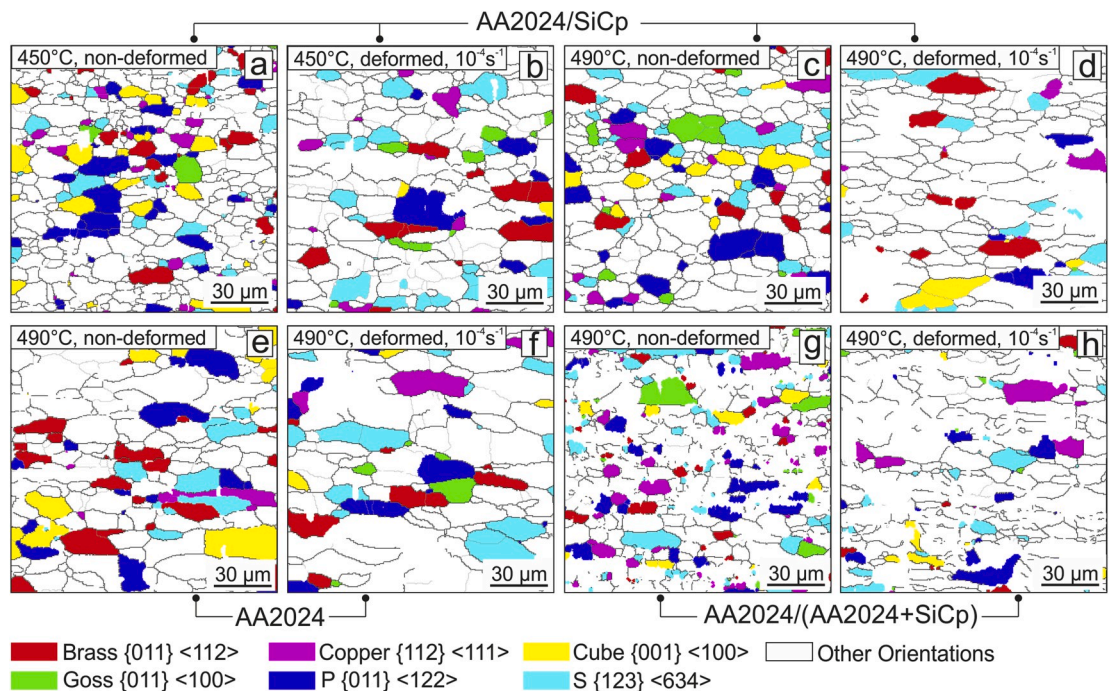

Fig. 7. EBSD orientation maps obtained after uniaxial tensile testing of the AA2024/SiC$_p$ samples (deformed and non-deformed regions) tested at strain rates of 10^{-4} s^{-1} at (a, b) 450 °C and (c, d) 490 °C; (e, f) AA2024 alloy, and (g, h) AA2024/(AA2024+SiC$_p$).

factors to the formation of microstructure and exhibited properties of MMCs.

The plots in Fig. 4a, d shows a significant effect of temperature on ductility of AA2024 matrix alloy. At a low strain rate (10^{-4} s^{-1}), the elongation increases with a rise of testing temperature from ~103.8 ±

16.7% (450 °C) to ~179.3 ± 28.4% (490 °C). Dissolution of Cu and Mg at higher temperatures explains this observation, which may result in their faster diffusion through the aluminum matrix [81]. As a result, a high ductility at low strain rates is provided by diffusional creep acting both as an individual process and as an accommodation mechanism for grain
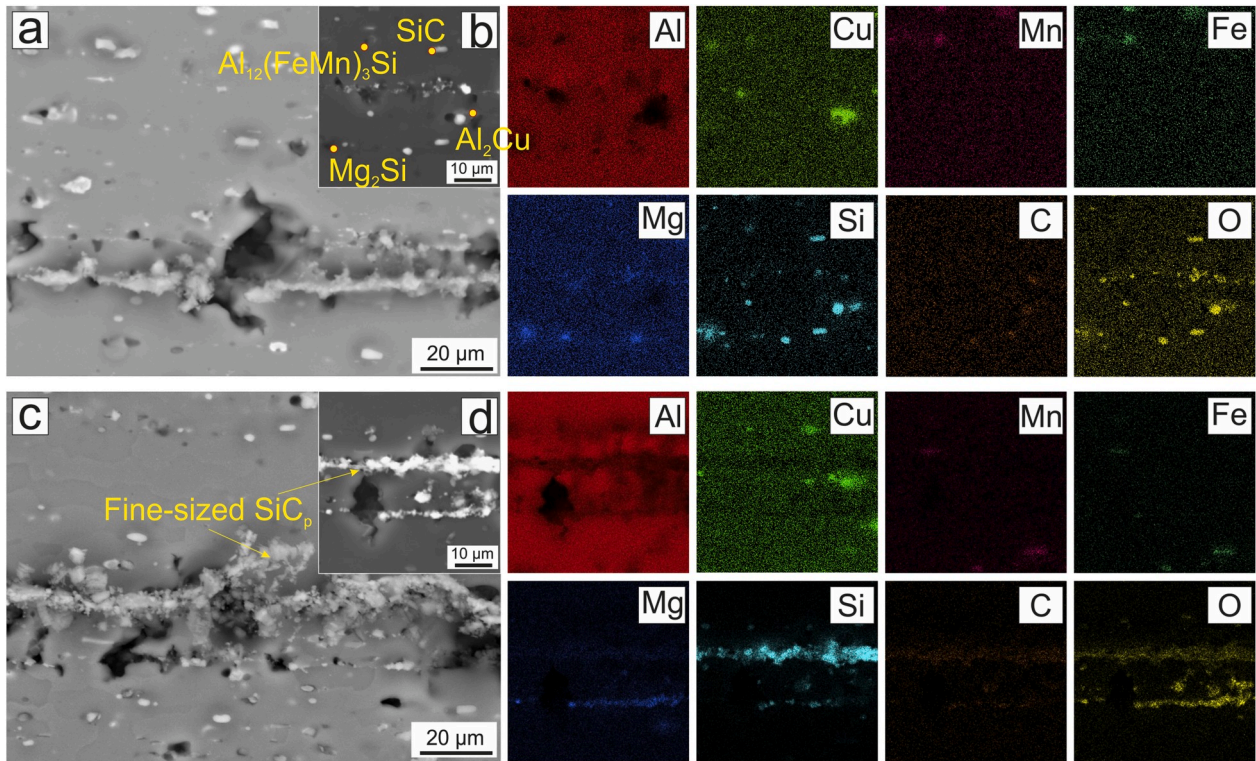
Fig. 8. Defects formed during the deformation of AA2024/SiC$_p$ (2 vol %) at 10^{-1} s^{-1} and 490°C: (a) SEM image and (b) EDS elemental maps.
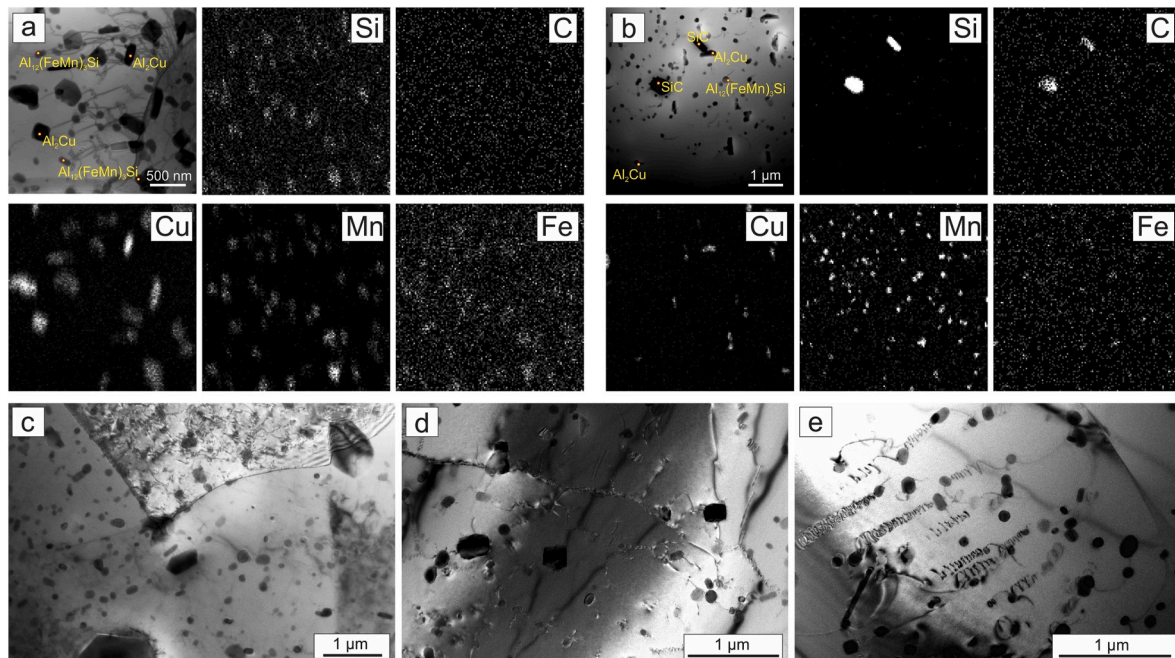

Fig. 9. STEM images and selected EDS element maps of AA2024/SiC$_p$ deformed at strain rates of (a) 10^{-1} s^{-1} and (b) 10^{-3} s^{-1} at 450 °C. Al and Mg element maps are not shown on the figure because of the uniform distribution of these elements in the observation area. BF TEM images were acquired from regions deformed at strain rates of (c) 10^{-2} s^{-1}, (d) 10^{-3} s^{-1}, and (e) 10^{-4} s^{-1}.

boundary sliding. The effect was clearly demonstrated in Refs. [81] by comparing the behavior of aluminum-based alloys with different concentrations of solutes. Owing to the continuous diffusion/deformation processes, further impact of high temperature results in the enhancement of microstructural changes (e.g. growth of second-phase particles). Thus, DGG (a deformation-induced process influenced by the migration

rate of grain boundaries which increases with temperature) becomes one of the factors that limits ductility.Whereas the temperature-related solute effect results in better performance of the matrix alloy, it does not explain the observed, significant increase in ductility of the MMC at the same testing conditions. Fig. 4b,e shows how the introduction of reinforcement components of a small volume fraction may result in
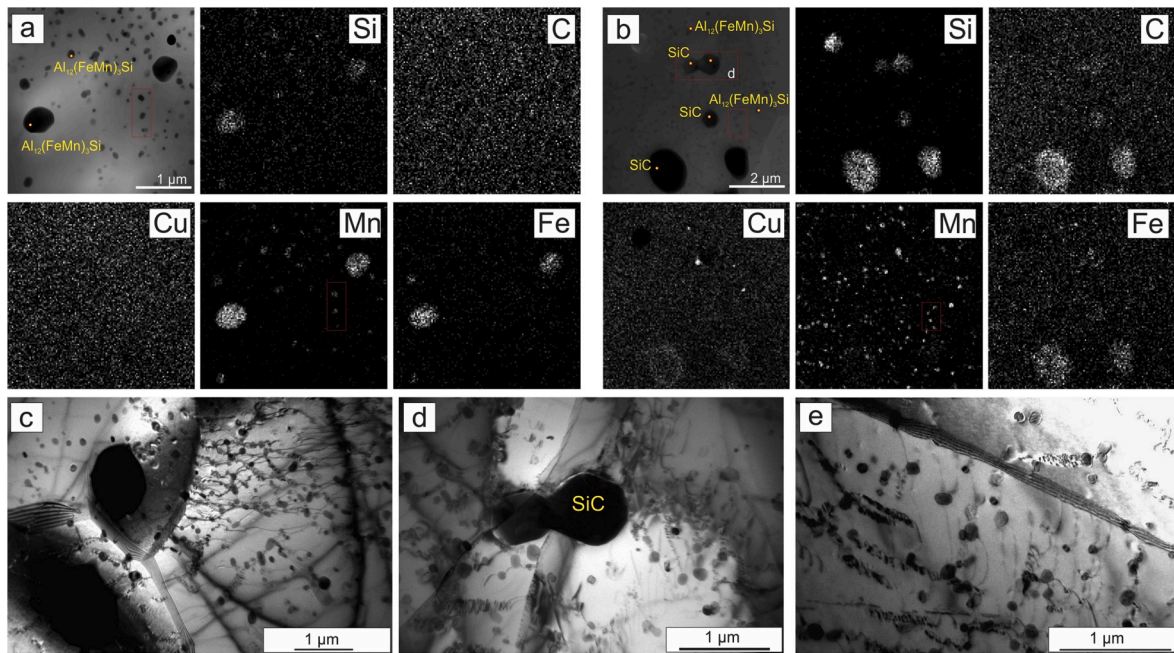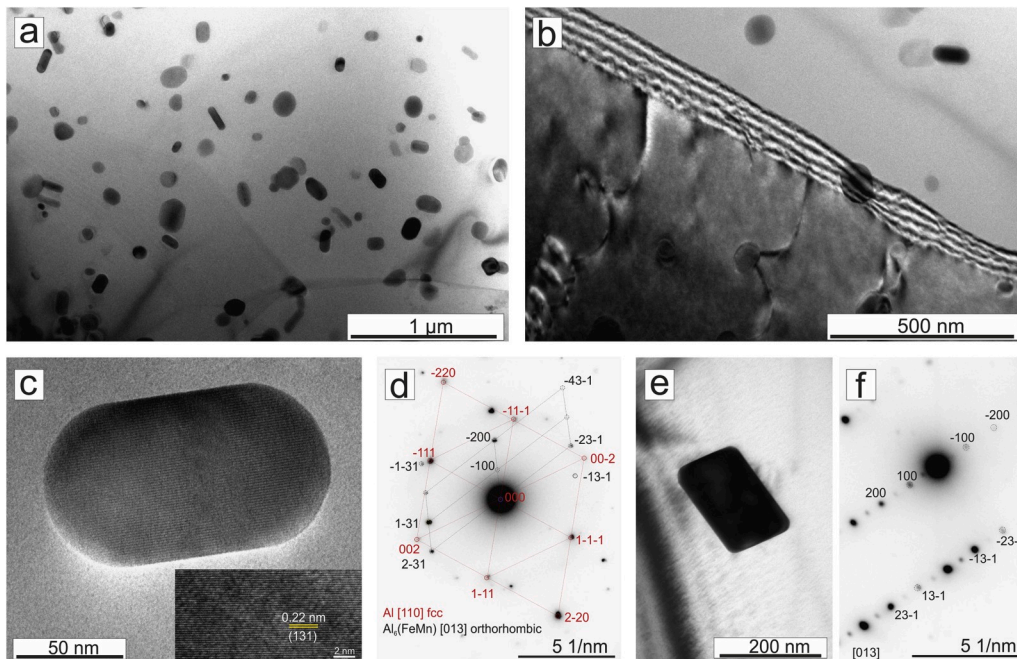
Fig. 10. (a, b) STEM images and selected EDS element maps of AA2024/SiC$_p$ deformed at strain rate of 10^{-1} s^{-1} at 490 °C. Al and Mg element maps are not shown on the figure owing to the uniform distribution of these elements in the observation area. BF TEM images were acquired from regions deformed at strain rates of (c, d) 10^{-1} s^{-1} and (e) 10^{-2} s^{-1}.

Fig. 11. BF TEM images of Al$_6$(FeMn) dispersoids: (a) non-deformed region, (b) pinning event at a grain boundary of a deformed region at 10^{-2} s^{-1}/490 °C, (c) high resolution TEM image of elliptical particle with related (d) SAEDs from the matrix and precipitate, (e, f) parallelogrammic particle and SAED.

increased elongation (252.7 ± 19.2%) at 10^{-4} s^{-1} (490 °C) in AA2024/SiC$_p$ (2 vol %) compared to those (179.3 ± 28.4%) for AA2024. We assume that both the refined microstructure and the resistance to grain growth provided by ceramic particles is responsible for this increase. We see certain confirmations of this assumption in research presented by Daehn [82] who states that there is a balance between the substructure refinement due to the flow and diffusional coarsening at elevated temperatures. Reinforcements in the matrix stabilize the substructure against coarsening and contribute to the lower grain growth rates. Based on a number of experimental evidences, Hassan et al. [83] pointed out that a key factor affecting the improvement in ductility of an aluminum alloy reinforced with SiC$_p$ is the degree of metal-working. A higher degree of reduction from metal-working helps to increase the composite ductility by reducing the matrix porosity, dispersing the reinforced particles more finely and breaking up the second-phase inclusions to more effectively disperse them. SiC by nature is characterized by a higher degree of size and phase stability in the given temperature interval. By contrast, hardening particles (e.g. θ-Al$_2$Cu and S–Al$_2$CuMg)

which form in the MMC matrix tend to increase in size and change in volume fraction. For example, straining of AA2024 at 490°C illustrates how gradual dissolution of Cu leads to a steady decrease of pinning pressure on migrating grain boundaries. Unlike AA2024, the presence of SiC particulates in AA2024/SiC$_p$ (2 vol %) compensates for the gradual disappearance of the second-phase particles, and subsequently slows down both static and DGG at high temperatures during deformation at low strain rates. The effect of SiC$_p$ on the static and DGG is noticeable from the data in Table 2, and by comparing EBSD maps acquired from the samples of AA2024/SiC$_p$ (Fig. 5d–f), AA2024 (Fig. 6a and b), and AA2024/(AA2024+SiC$_p$) (Fig. 6c and d) deformed at a strain rate of 10^{-4} s^{-1} (490 °C).

Reinforcements may have a positive effect on grain microstructure at lower temperatures as well due to insignificant size changes, whereas second-phase particles demonstrate a size increase due to Ostwald ripening (when a thermodynamically unstable two-phase system reduces its total energy by means of increase in the mean size of the second phase) [84,85] and/or as a result of strain-induced particle coarsening [70]. This changes the ratio in the pinning (drag) pressure (P_Z) exerted by the spherical particles of a radius r and volume fraction f_v on a unit area of the boundary by $P_Z = \frac{3 \times f_v \times \gamma}{2 \times r}$, where γ is the average boundary energy of the system. It leads to a decrease of pinning force on migrating grain boundaries and an increase of the mean grain size following the Zener equation ($D_Z = A\frac{r}{f_v}$, where D_Z is the Zener limiting grain size in normal grain growth and A is a proportionality coefficient) [86]. Embedding thermodynamically stable ceramic particles, which are to a less extent subject to changes and are able to retain their initial properties, can be considered as an additional opportunity to design a grain structure with predictable behavior and properties.

In addition to the temperature effect on secondary phases and grain growth, an important time-dependent factor – strain rate – has a significant effect on the development of substructure and crack propagation. A low-temperature deformation results in intensive development of substructure. The percentage of low-angle grain boundaries is used as an indicator of substructure development. It is worth noting that dislocations are formed in large amounts during deformation at high strains. However, they are generally not represented during analysis of EBSD maps to eliminate data distortion due to the presence of surface relief (boundaries below misorientation angles of 2° were not taken into account during substructure measurements). Their migration is partially limited by both fine-sized reinforcements and dispersoids. The stored energy of the formed substructure has an additional effect on the rate of migration of HAGBs. At low strain rates and high temperatures stresses in the material are low, thus the mechanism of deformation is controlled by grain boundary sliding and dislocation creep. The dislocation density also remains low due to faster recovery, and the failure of the material is influenced by the steady increase in stresses caused by grain growth. At high strain rates, when stresses sharply increase, the formation and propagation of cracks become the dominant factors for material failure.

Despite the fact that AA2024 alloy has a good combination of characteristics, such as fracture toughness and resistance to fatigue crack growth [50], the introduction of reinforcement particles at the right volume fraction is likely to have additional beneficial effect on fatigue behavior. The morphology, size, and volume fraction of reinforcements become especially important when studying the fatigue characteristics of MMC. Experimental data presented in Ref. [87] show that an increase in volume fraction of ceramic reinforcements reduces ductility and fracture toughness. When considering this effect separately, the deterioration in properties can be explained by brittle fracture of large reinforcement particles. Large reinforcements (and especially their agglomerates) may become the sources for crack origination due to a weak connection at the matrix-reinforcement interface. The reduction in particle size provides an improvement in tensile ductility. The smaller reinforcing particles cavitate less easily than their larger counterparts. As a result, an MMC containing small-sized

reinforcements can accommodate greater strains. The effects of particle size on the fracture toughness in SiC$_p$/Al–Cu–Mg are clearly shown in Ref. [88]. In addition, the lower rates of work hardening tend to reduce the flow stress and facilitate an improvement in the fracture toughness. The positive effect of fine-sized particles on fatigue strength is shown in Ref. [83]. The evidence also indicates that reinforcement improves not only the stress-controlled fatigue behavior, but also the resistance to fatigue crack propagation. At the same time, the matrix reinforced with low volume fractions prevents propagation of cracks. In this regard, the formation of a large number of closed cracks and interface voids results in a more uniform distribution of stress in the matrix, and subsequently extends cracking resistance of AA2024/SiC$_p$ (2 vol %) during deformation at high strain rates. At low strain rates the same effect provides more uniform deformation, preventing the extensive development of new, large cracks and the propagation of existing ones.

On the basis of the data obtained in this study, industrial prospects for using MMCs with embedded, fine-sized reinforcements of a low volume fraction appear promising, as they exhibit the following beneficial features: (a) the formation of a fine-grained structure and reduction of static and DGG rates, (b) ensuring a large degree of elongation of MMCs at high strain rates, (c) positive effect of reinforcements and solutes on ductility of MMCs at elevated temperatures in comparison with the matrix alloy, (d) inhibition of crack propagation by a low volume fraction of the reinforcements. This represents both an opportunity to point out the improved properties of MMCs of interest, and to optimize the technological parameters of production such as scalable production methods, thermomechanical treatments, and optimization of volume fractions. An example is the formation of materials under superplastic conditions, where a superplastic matrix modified by reinforcements with a low sensitivity to forming conditions can exhibit the required plastic characteristics in the optimal temperature and strain rate regimes.

5. Conclusions

The addition of a low volume fraction (2%) of fine-sized SiC$_p$ reinforcements to AA2024 commercial alloy was shown to enhance both ductility and cracking resistance at elevated temperatures at low strain rates. Liquid-state fabrication in the semisolid temperature interval enhances the embedding of powder by changing the rheological properties of the melt. As an alternative, mechanically alloyed granules are shown to be promising "delivery agents" to uniformly distribute reinforcements. Thermomechanical processing of MMCs facilitates the formation of a finer grain structure due to the positive effect of particle stimulated nucleation (PSN) and the restraining effect of reinforcements on the growth of recrystallized grains. The positive effect is expressed in as higher ductility of the AA2024/SiC$_p$ while retaining similar strength and toughness of the matrix alloy alone. The baseline, high ductility in the matrix alloy is due to the solute effect and high density of dispersoids restraining grain boundary movement, whereas the major contribution of SiC$_p$ is likely due to a lower rate of DGG. This provides a better control of microstructural changes and compensates dissolution or temperature/deformation-induced coarsening of constituent phases. A positive effect of SiC$_p$ is manifested as an additional barrier to the propagation of cracks, leading to large material elongations at high strain rates. This fact can have a positive influence during fatigue loads, as well as in the case of optimization of forming regimes. Further work to optimize processing conditions, dispersoid volume fractions, and thermomechanical treatment is likely to expand the benefits and operating envelope of Al-based MMCs.

Declaration of competing interest

The authors declare that they have no known competing financial interests or personal relationships that could have appeared to influence the work reported in this paper.

CRediT authorship contribution statement

O.V. Rofman: Investigation, Formal analysis, Writing - original draft. **A.V. Mikhaylovskaya:** Conceptualization, Formal analysis, Supervision. **A.D. Kotov:** Investigation, Resources. **A.G. Mochugovskiy:** Investigation. **A.K. Mohamed:** Investigation. **V.V. Cheverikin:** Investigation. **M.P. Short:** Formal analysis, Writing - review & editing.

Acknowledgment

Appendix A. Supplementary data

Supplementary data to this article can be found online at https://doi.org/10.1016/j.msea.2020.139697.

References

[1] X. Ma, Y.F. Zhao, W.J. Tian, Z. Qian, H.W. Chen, Y.Y. Wu, X.F. Liu, A novel Al matrix composite reinforced by nano-AlNp network, Sci. Rep. 6 (2016) 1–8, https://doi.org/10.1038/srep34919.

[2] J. Li, G. Zhao, S. Wu, Z. Huang, S. Lü, Q. Chen, F. Li, Preparation of hybrid particulates SiCnp and Mg2Si reinforced Al-Cu matrix composites, Mater. Sci. Eng., A 751 (2019) 107–114, https://doi.org/10.1016/J.MSEA.2019.02.076.

[3] J. Gu, Y. Huang, K.U. Kainer, N. Hort, Role of sic in grain refinement of aluminum-free Mg-Zn alloys, in: A. Singh, K. Solanki, M. v Manuel, N.R. Neelameggham (Eds.), Magnesium Technology 2016, John Wiley & Sons, Inc., Hoboken, NJ, USA, 2016, pp. 177–181, https://doi.org/10.1002/9781119274803.ch36.

[4] P. Xiao, Y. Gao, F. Xu, S. Yang, B. Li, Y. Li, Z. Huang, Q. Zheng, An investigation on grain refinement mechanism of TiB2 particulate reinforced AZ91 composites and its effect on mechanical properties, J. Alloys Compd. 780 (2019) 237–244, https://doi.org/10.1016/J.JALLCOM.2018.11.253.

[5] T.W. Clyne, P.J. Withers, An Introduction to Metal Matrix Composites, Cambridge University Press, Cambridge, 1993, https://doi.org/10.1017/CBO9780511623080.

[6] D.B. Miracle, Metal matrix composites - from science to technological significance, Compos. Sci. Technol. 65 (2005) 2526–2540, https://doi.org/10.1016/j.compscitech.2005.05.027.

[7] Metal-matrix composites innovations, advances and applications, in: T.S. Srivatsan, Y. Zhang, W.C. Harrigan (Eds.), An SMD Symposium in Honor of William C. Harrigan, Jr., first ed., Springer International Publishing, 2018, p. 250, https://doi.org/10.1007/978-3-319-72853-7.

[8] M.J. Koczak, M.K. Premkumar, Emerging technologies for the in-situ production of MMCs, JOM (J. Occup. Med.) 45 (1993) 44–48, https://doi.org/10.1007/BF03223365.

[9] K.P. So, X. Liu, H. Mori, A. Kushima, J.G. Park, H.S. Kim, S. Ogata, Y.H. Lee, J. Li, Ton-scale metal–carbon nanotube composite: the mechanism of strengthening while retaining tensile ductility, Extreme Mech. Lett. 8 (2016) 245–250, https://doi.org/10.1016/J.EML.2016.04.002.

[10] R.I. González, F. Valencia, J. Mella, A.C.T. van Duin, K.P. So, J. Li, M. Kiwi, E. M. Bringa, Metal-nanotube composites as radiation resistant materials, Appl. Phys. Lett. 109 (2016), 33108, https://doi.org/10.1063/1.4959246.

[11] A. Aversa, G. Marchese, M. Lorusso, F. Calignano, S. Biamino, E.P. Ambrosio, D. Manfredi, P. Fino, M. Lombardi, M. Pavese, Microstructural and mechanical characterization of aluminum matrix composites produced by laser powder bed fusion, Adv. Eng. Mater. 19 (2017) 1–11, https://doi.org/10.1002/adem.201700180.

[12] E. Fereiduni, M. Yakout, M. Elbestawi, Laser-based additive manufacturing of lightweight metal matrix composites, in: B. AlMangour (Ed.), Additive Manufacturing of Emerging Materials, Springer International Publishing, Cham, 2019, pp. 55–109, https://doi.org/10.1007/978-3-319-91713-9_3.

[13] A. Kitt, EWI accelerates 3D printing of metal matrix composites. https://ewi.org/ewi-accelerates-3d-printing-of-metal-matrix-composites-new-article/, 2016 (accessed March 29, 2019).

[14] A. Bloyce, J.C. Summers, Static and dynamic properties of squeeze-cast A357-SiC particulate Duralcan metal matrix composite, Mater. Sci. Eng., A 135 (1991) 231–236, https://doi.org/10.1016/0921-5093(91)90568-8.

[15] P. Wycliffe, Galling in aluminum alloys and Duralcan aluminum matrix composites, Wear 162–164 (1993) 574–579, https://doi.org/10.1016/0043-1648(93)90543-U.

[16] D. Hashiguchi, D. Tricker, A. Tarrant, J. Campbell, C. Pokross, Discontinuously reinforced aluminum MMC extrusions, Met. Powder Rep. 72 (2017) 252–258, https://doi.org/10.1016/J.MPRP.2016.01.074.

[17] N.D. Tricker, A.D. Tarrant, R.v. Michel, J.R. Clune, Light Weight High Stiffness Metal Composite, US20160303649A1, 2016.

[18] J. Falsafi, M. Rosochowska, P. Jadhav, D. Tricker, Lower cost automotive piston from 2124/SiC/25p metal-matrix composite, SAE Int. J. Engines 10 (2017) 1984–1992, https://doi.org/10.4271/2017-01-1048.

[19] N. Bailey, Aluminium matrix composites, Reinforc Plast (2019), https://doi.org/10.1016/j.repl.2019.01.004.

[20] W.C. Harrigan, A.W. Sommer, Incorporation of Nano-Size Particles into Aluminum or Other Light Metals by Decoration of Micron Size Particles, 2018. US10058917B2.

[21] M. Currelli, W.C. Harrigan Jr., A.W. Sommer, Equipartition of Nano Particles in a Metallic Matrix to Form a Metal Matrix Composite (MMC), 2018. US20180029119A1.

[22] Y. Nishida, Introduction to metal matrix composites. https://doi.org/10.1007/978-4-431-54237-7, 2013.

[23] D.S. Han, H. Jones, H. v Atkinson, The wettability of silicon carbide by liquid aluminium: the effect of free silicon in the carbide and of magnesium, silicon and copper alloy additions to the aluminium, J. Mater. Sci. 28 (1993) 2654–2658, https://doi.org/10.1007/BF00356199.

[24] B. Previtali, Metal matrix composites: casting processes, in: Wiley Encyclopedia of Composites, John Wiley & Sons, Inc., Hoboken, NJ, USA, 2012, https://doi.org/10.1002/9781118097298.weoc138.

[25] F. Zhang, P. Sun, X. Li, G. Zhang, A comparative study on microplastic deformation behavior in a SiCp/2024Al composite and its unreinforced matrix alloy, Mater. Lett. 49 (2001) 69–74, https://doi.org/10.1016/S0167-577X(00)00344-X.

[26] G. Wu, X. Wang, L. Jiang, B. Ma, A nanostructural design to produce high ductility of high volume fraction SiCp/Al composites with enhanced strength, Mater. Des. 61 (2014) 141–145, https://doi.org/10.1016/j.matdes.2014.04.048.

[27] S. Jayalakshmi, M. Gupta, Metallic amorphous alloy reinforcements in light metal matrices. https://doi.org/10.1007/978-3-319-15016-1, 2015.

[28] S. Jayalakshmi, M. Gupta, Light Metal Matrix Composites, Springer International Publishing, Cham, 2015, https://doi.org/10.1007/978-3-319-15016-1_2.

[29] Y. Yang, J. Lan, X. Li, Study on bulk aluminum matrix nano-composite fabricated by ultrasonic dispersion of nano-sized SiC particles in molten aluminum alloy, Mater. Sci. Eng. 380 (2004) 378–383, https://doi.org/10.1016/j.msea.2004.03.073.

[30] A.V. Pozdniakov, A. Lotfy, A. Qadir, E. Shalaby, M.G. Khomutov, A.Yu Churyumov, V.S. Zolotorevskiy, Development of Al-5Cu/B4C composites with low coefficient of thermal expansion for automotive application, Mater. Sci. Eng. 688 (2017) 1–8, https://doi.org/10.1016/J.MSEA.2017.01.075.

[31] A.V. Pozdniakov, V.S. Zolotorevskiy, R.Yu Barkov, A. Lotfy, A.I. Bazlov, Microstructure and material characterization of 6063/B4C and 1545K/B4C composites produced by two stir casting techniques for nuclear applications, J. Alloys Compd. 664 (2016) 317–320, https://doi.org/10.1016/J.JALLCOM.2015.12.228.

[32] T. Lin, C. Tan, B. Liu, A. McDonald, Microstructure of AA2024-SiC nanostructured metal matrix composites, J. Mater. Sci. 43 (2008) 7507–7512, https://doi.org/10.1007/s10853-008-2726-7.

[33] E. Dagasan, E. Gercekcioglu, S. Unalan, Characterization of Al matrix SiC reinforced sub-micron composites produced by mechanical alloying, J. Powder Metall. Min. (2017) 6–11, https://doi.org/10.4172/2168-9806.1000164, 06.

[34] D. Wei, R. Dave, R. Pfeffer, Mixing and characterization of nanosized powders: an assessment of different techniques, J. Nanoparticle Res. 4 (2002) 21–41, https://doi.org/10.1023/A:1020184524538.

[35] B. Li, Y. Lin, F. Chen, L. Zhang, E.J. Lavernia, Spray forming of MMCs, in: Reference Module in Materials Science and Materials Engineering, Elsevier, 2016, https://doi.org/10.1016/B978-0-12-803581-8.03715-2.

[36] C. Si, X. Tang, X. Zhang, J. Wang, W. Wu, Microstructure and mechanical properties of particle reinforced metal matrix composites prepared by gas-solid two-phase atomization and deposition technology, Mater. Lett. 201 (2017) 78–81, https://doi.org/10.1016/J.MATLET.2017.04.150.

[37] D. Ghanbari, M. Kasiri Asgarani, K. Amini, F. Gharavi, Influence of heat treatment on mechanical properties and microstructure of the Al2024/SiC composite produced by multi–pass friction stir processing, Measurement 104 (2017) 151–158, https://doi.org/10.1016/J.MEASUREMENT.2017.03.024.

[38] N.H. Loh, S.B. Tor, K.A. Khor, Production of metal matrix composite part by powder injection molding, J. Mater. Process. Technol. 108 (2001) 398–407, https://doi.org/10.1016/S0924-0136(00)00855-4.

[39] X.G. Qiao, T. Ying, M.Y. Zheng, E.D. Wei, K. Wu, X.S. Hu, W.M. Gan, H. G. Brokmeier, I.S. Golovin, Microstructure evolution and mechanical properties of nano-SiCp/AZ91 composite processed by extrusion and equal channel angular pressing (ECAP), Mater. Char. 121 (2016) 222–230, https://doi.org/10.1016/j.matchar.2016.10.003.

[40] M. Hosseini, A. Yazdani, H. Danesh Manesh, Al 5083/SiCp composites produced by continual annealing and roll-bonding, Mater. Sci. Eng. 585 (2013) 415–421, https://doi.org/10.1016/j.msea.2013.07.077.

[41] R. Jamaati, M.R. Toroghinejad, A. Najafizadeh, Application of anodizing and CAR processes for manufacturing Al/Al2O3 composite, Mater. Sci. Eng. 527 (2010) 3857–3863, https://doi.org/10.1016/j.msea.2010.02.052.

[42] F.J. Humphreys, W.S. Miller, M.R. Djazeb, Microstructural development during thermomechanical processing of particulate metal-matrix composites, Mater. Sci. Technol. 6 (1990) 1157–1166, https://doi.org/10.1179/026708390790189975.

[43] W.S. Miller, F.J. Humphreys, Strengthening mechanisms in particulate metal matrix composites, Scripta Metall. Mater. 25 (1991) 33–38, https://doi.org/10.1016/0956-716X(91)90349-6.

[44] P.B. Prangnell, T. Downes, W.M. Stobbs, P.J. Withers, The deformation of discontinuously reinforced MMCs—I. The initial yielding behaviour, Acta Metall. Mater. 42 (1994) 3425–3436, https://doi.org/10.1016/0956-7151(94)90475-8.

[45] P.B. Prangnell, T. Downes, P.J. Withers, W.M. Stobbs, The deformation of discontinuously reinforced MMCs—II. The elastic response, Acta Metall. Mater. 42 (1994) 3437–3442, https://doi.org/10.1016/0956-7151(94)90476-6.

[46] B.C. Ko, G.S. Park, Y.C. Yoo, Effects of SiC particle volume fraction on the microstructure and hot workability of SiCp/AA 2024 composites, J. Mater. Process. Technol. 95 (1999) 210–215, https://doi.org/10.1016/S0924-0136(99)00292-7.

[47] G.H. Zahid, R.I. Todd, P.B. Prangnell, Deformation and microstructural development in a 2124Al/SiCₚMMC during high strain rate superplasticity, Mater. Sci. Forum 304–306 (2009) 233–240. https://doi.org/10.4028/www.scientific.net/msf.304-306.233.

[48] G.H. Zahid, R.I. Todd, P.B. Prangnell, Superplasticity in an alulllinium alloy 2124/SiC p composite, Mater. Sci. Technol. 14 (1998) 901–905, https://doi.org/10.1179/mst.1998.14.9-10.901.

[49] T.G. Nieh, J. Wadsworth, O.D. Sherby, Superplasticity in Metals and Ceramics, Cambridge University Press, Cambridge, 1997, https://doi.org/10.1017/CBO9780511525230.

[50] S.G. Alieva, M.B. Altman, S.M. Ambartsumyan, Promyshlennye Aluminievye Splavy [Industrial Aluminum Alloys], second ed., Metallurgiya, Moscow, 1984.

[51] J.R. Davis (Ed.), Corrosion of Aluminum and Aluminum Alloys, ASM International, 1999.

[52] M. Kök, K. Özdin, Wear resistance of aluminium alloy and its composites reinforced by Al2O3 particles, J. Mater. Process. Technol. 183 (2007) 301–309, https://doi.org/10.1016/j.jmatprotec.2006.10.021.

[53] F.J. Humphreys, Review Grain and subgrain characterisation by electron backscatter diffraction, J. Mater. Sci. 36 (2001) 3833–3854, https://doi.org/10.1023/A:1017973432592.

[54] EBSD post-processing software. https://nano.oxinst.com/products/ebsd/, 2019. (Accessed 25 February 2019), in: https://nano.oxinst.com/products/ebsd/post-processing-software.

[55] M.C. Flemings, Behavior of metal alloys in the semisolid state, Metall. Trans., B 22 (1991) 269–293, https://doi.org/10.1007/BF02651227.

[56] F.A. Girot, J.M. Quenisset, R. Naslain, Discontinuously-reinforced aluminum matrix composites, Compos. Sci. Technol. 30 (1987) 155–184, https://doi.org/10.1016/0266-3538(87)90007-8.

[57] E. Evangelista, Hot Deformation and Processing of Aluminum Alloys, first ed., CRC Press, 2011 https://doi.org/10.1201/b11227.

[58] M.P. Thomas, Improvement of the mechanical properties of 2124 Al/SiCp MMC plate by optimisation of the solution treatment, Compos. Sci. Technol. 56 (1996) 1141–1149, https://doi.org/10.1016/S0266-3538(96)00077-2.

[59] V. Laurent, D. Chatain, N. Eustathopoulos, Wettability of SiO2 and oxidized SiC by aluminium, Mater. Sci. Eng., A 135 (1991) 89–94, https://doi.org/10.1016/0921-5093(91)90542-U.

[60] V. Laurent, C. Rado, N. Eustathopoulos, Wetting kinetics and bonding of Al and Al alloys on α-SiC, Mater. Sci. Eng., A 205 (1996) 1–8, https://doi.org/10.1016/0921-5093(95)09896-8.

[61] D.J. Lloyd, H. Lagace, A. McLeod, P.L. Morris, Microstructural aspects of aluminium-silicon carbide particulate composites produced by a casting method, Mater. Sci. Eng., A 107 (1989) 73–80, https://doi.org/10.1016/0921-5093(89)90376-6.

[62] T. Iseki, T. Kameda, T. Maruyama, Interfacial reactions between SiC and aluminium during joining, J. Mater. Sci. 19 (1984) 1692–1698, https://doi.org/10.1007/BF00563067.

[63] S.W. Lai, D.D.L. Chung, Phase distribution and associated mechanical property distribution in silicon carbide particle-reinforced aluminium fabricated by liquid metal infiltration, J. Mater. Sci. 29 (1994) 2998–3016, https://doi.org/10.1007/BF01117613.

[64] S.W. Lai, D.D.L. Chung, Fabrication of particulate aluminium-matrix composites by liquid metal infiltration, J. Mater. Sci. 29 (1994) 3128–3150, https://doi.org/10.1007/BF00356655.

[65] O.V. Rofman, A.V. Mikhaylovskaya, A.D. Kotov, A.S. Prosviryakov, V.K. Portnoy, Effect of thermomechanical treatment on properties of an extruded Al-3.0Cu-1.2Mg/SiCp composite, Mater. Sci. Eng., A 739 (2019) 235–243, https://doi.org/10.1016/J.MSEA.2018.10.053.

[66] S. Hashmi, C.J. van Tyne, G.F. Batalha, B. Yilbas (Eds.), Comprehensive Materials Processing, Elsevier, 2014.

[67] Y.L. Liu, A study on flow stress of Al-SiC composites deformed in a large range of strain, Scripta Mater. 35 (1996) 253–259, https://doi.org/10.1016/1359-6462(96)00117-0.

[68] C. Badini, F. Marino, E. Verné, Calorimetric study on precipitation path in 2024 alloy and its SiC composite, Mater. Sci. Eng. 191 (1995) 185–191, https://doi.org/10.1016/0921-5093(94)09637-C.

[69] K.B. Hyde, P.S. Bate, Dynamic grain growth in Al–6Ni: modelling and experiments, Acta Mater. 53 (2005) 4313–4321, https://doi.org/10.1016/J.ACTAMAT.2005.05.029.

[70] O.V. Rofman, P.S. Bate, Dynamic grain growth and particle coarsening in Al-3.5Cu, Acta Mater. 58 (2010), https://doi.org/10.1016/j.actamat.2009.12.039.

[71] P. Bate, The effect of deformation on grain growth in Zener pinned systems, Acta Mater. 49 (2001) 1453–1461, https://doi.org/10.1016/S1359-6454(01)00033-7.

[72] M. Hillert, Inhibition of grain growth by second-phase particles, Acta Metall. 36 (1988) 3177–3181, https://doi.org/10.1016/0001-6160(88)90053-3.

[73] C.K.S. Moy, M. Weiss, J. Xia, G. Sha, S.P. Ringer, G. Ranzi, Influence of heat treatment on the microstructure, texture and formability of 2024 aluminium alloy, Mater. Sci. Eng., A 552 (2012) 48–60, https://doi.org/10.1016/J.MSEA.2012.04.113.

[74] A. Poudens, B. Bacroix, T. Bretheau, Influence of microstructures and particle concentrations on the development of extrusion textures in metal matrix composites, Mater. Sci. Eng., A 196 (1995) 219–228, https://doi.org/10.1016/0921-5093(94)09703-8.

[75] J. Roy, S. Chandra, S. Das, S. Maitra, Oxidation behaviour of silicon carbide-a review, Adv. Mater. Sci. 38 (2014) 29–39. http://www-proxy.ipme.ru/e-journals/RAMS/no_13814/04_13814_roy.pdf.

[76] S. Wu, N. Claussen, Reaction bonding and mechanical properties of mullite/silicon carbide composites, J. Am. Ceram. Soc. 77 (1994) 2898–2904, https://doi.org/10.1111/j.1151-2916.1994.tb04521.x.

[77] N.A. Belov, N.N. Avksent'eva, Quantitative analysis of the Al – Cu – Mg – Mn – Si phase diagram as applied to commercial aluminum alloys of series 2xxx, Met. Sci. Heat Treat. 55 (2013) 358–363, https://doi.org/10.1007/s11041-013-9635-3.

[78] E.A. Starke, J.T. Staley, Application of modern aluminum alloys to aircraft, Prog. Aero. Sci. 32 (1996) 131–172, https://doi.org/10.1016/0376-0421(95)00004-6.

[79] A.E. Hughes, R. Parvizi, M. Forsyth, Microstructure and corrosion of AA2024, Corrosion Rev. 33 (2015) 1–30, https://doi.org/10.1515/corrrev-2014-0039.

[80] A. Boag, A.E. Hughes, N.C. Wilson, A. Torpy, C.M. MacRae, A.M. Glenn, T. H. Muster, How complex is the microstructure of AA2024-T3? Corrosion Sci. 51 (2009) 1565–1568, https://doi.org/10.1016/J.CORSCI.2009.05.001.

[81] K. Sotoudeh, P.S. Bate, Diffusion creep and superplasticity in aluminium alloys, Acta Mater. 58 (2010) 1909–1920, https://doi.org/10.1016/J.ACTAMAT.2009.11.034.

[82] G.S. Daehn, 4.9 microstructural design of metal matrix composites for high temperature strength and superplastic behavior by strain mismatch, Comprehen. Composite Mater. II (2018) 242–274, https://doi.org/10.1016/B978-0-12-803581-8.09966-5.

[83] H.A. Hassan, J.J. Lewandowski, 4.4 fracture toughness and fatigue of particulate metal matrix composites, Compr. Compos. Mater. II (2018) 86–136, https://doi.org/10.1016/B978-0-12-803581-8.09964-1.

[84] W.L. Noorduin, E. Vlieg, R.M. Kellogg, B. Kaptein, From Ostwald ripening to single chirality, Angew. Chem. Int. Ed. 48 (2009) 9600–9606, https://doi.org/10.1002/anie.200905215.

[85] L. Ratke, P.W. Voorhees, Growth and coarsening. Ostwald Ripening in Material Processing, first ed., Springer-Verlag Berlin Heidelberg, Berlin, Heidelberg, 2002 https://doi.org/10.1007/978-3-662-04884-9.

[86] P.A. Manohar, M. Ferry, T. Chandra, Five decades of the zener equation, ISIJ Int. 38 (1998) 913–924, https://doi.org/10.2355/isijinternational.38.913.

[87] Y. Sugimura, S. Suresh, Effects of SiC content on fatigue crack growth in aluminum alloys reinforced with SiC particles, Metall. Trans., A 23 (1992) 2231–2242, https://doi.org/10.1007/BF02646016.

[88] M. Song, B. Huang, Effects of particle size on the fracture toughness of SiCp/Al alloy metal matrix composites, Mater. Sci. Eng., A 488 (2008) 601–607, https://doi.org/10.1016/j.msea.2008.03.022.